Supplement of

Seasonal variations in photooxidant formation and light absorption in aqueous extracts of ambient particles

Lan Ma[1a], Reed Worland[1b], Laura Heinlein[1], Chrystal Guzman[1c], Wenqing Jiang[2], Christopher Niedek[2], Keith J. Bein[3], Qi Zhang[2], Cort Anastasio[1]

[1]Department of Land, Air and Water Resources, University of California, Davis, One Shields Avenue, Davis, CA 95616-8627, USA

[2]Department of Environmental Toxicology, University of California, Davis, One Shields Avenue, Davis, CA 95616-8627, USA

[3]Center for Health and the Environment, University of California, Davis, One Shields Avenue, Davis, CA 95616-8627, USA

[a]Now at: SGS-CSTC Standards Technical Services Co.,Ltd. Hangzhou Branch, Hangzhou, Zhejiang Province, 310052, China

[b]Now at: Department of Chemistry, University of Washington, WA, USA

[c]Now at: Department of Pharmacology, University of Washington, WA, USA

Correspondence to: Cort Anastasio (canastasio@ucdavis.edu)

Table of contents

Table S1. Particle collection and PME sample information

Sample Type	Sample ID	Collection dates[a]	Sampling duration (days)	Average $PM_{2.5}$ conc.[b] ($\mu g/m^3$)	PME particle mass/water ratio[c] (10^{-4} μg PM/μg H_2O)	α_{300}[d] (cm^{-1})	α_{365}[e] (cm^{-1})	R_{abs} (300-450 nm) (10^{-6} mol-photons $L^{-1}s^{-1}$)[f]	AAE[g]	E_2/E_3[h]	MAC_{DOC} (300 nm) (m^2 (g C)$^{-1}$)[i]	MAC_{DOC} (365 nm) (m^2 (g C)$^{-1}$)[i]	DOC (mg C L^{-1})	Light screening factor[j] PME	Light screening factor[j] PME+DMB
Winter & Spring	PME-111519	11/12/19-11/19/19	7.00	13.2	9.1 (0.3)	1.534	0.431	25	7.59	7.45	1.82	0.52	192	0.67	0.59
	PME-120319	12/3/19	1.00	10.6	1.2 (0.2)	0.112	0.027	1.6	8.17	8.84	1.57	0.40	16	0.97	0.75
	PME-122019	12/17/19-12/24/19	7.01	9.0	5.4 (0.4)	0.718	0.206	12	7.64	7.37	2.33	0.69	69	0.82	0.69
	PME-010220	1/2/20	1.01	10.2	1.1 (0.1)	0.116	0.031	1.8	7.78	8.28	1.54	0.43	17	0.97	0.75
	PME-010620	1/3/20-1/10/20	7.01	10.0	6.2 (0.5)	0.552	0.144	8.4	7.57	8.65	1.92	0.52	64	0.86	0.71
	PME-021620[k]	2/5/20-2/28/20	7.07	9.1	4.6 (0.5)	0.868	0.269	16	7.21	7.16	2.08	0.65	95	0.60	0.53
	PME-022020	2/20/20	1.00	9.0	0.89 (0.10)	0.231	0.070	4.1	7.26	6.91	2.50	0.76	21	0.94	0.75
	PME-030420	3/4/20	1.01	8.4	1.2 (0.2)	0.090	0.022	1.3	8.05	9.61	1.27	0.32	16	0.98	0.75
Summer & Fall	PME-070720	7/7/20	0.99	7.0	1.0 (0.2)	0.039	0.009	0.50	8.77	10.9	0.74	0.18	12	0.99	0.75
	PME-080420	8/4/20	1.01	7.2	0.79 (0.14)	0.019	0.004	0.22	8.97	17.0	0.43	0.09	9.9	1.00	0.75
	PME-101520	10/15/20	1.00	7.9	0.66 (0.25)	0.017	0.004	0.18	9.63	13.3	0.78	0.16	5.0	1.00	0.75
Fresh wildfire	PME-081920	8/19/20	0.99	67.9	3.7 (0.3)	1.960	0.812	43	7.26	4.22	3.82	1.59	118	0.55	0.50
	PME-082220[k]	8/21/20-8/24/20	1.20	49.3	4.1 (0.1)	2.017	0.653	38	7.15	6.50	3.10	1.00	150	0.78	0.67
	PME-082420	8/24/20	0.92	57.2	3.1 (0.2)	1.511	0.540	29	7.57	5.00	3.32	1.19	105	0.64	0.57
	PME-090920	9/9/20	1.00	44.6	3.0 (0.2)	0.871	0.259	15	7.42	7.46	2.90	0.86	69	0.78	0.67
Aged wildfire	PME-090120	9/1/20	0.99	19.2	1.4 (0.1)	0.199	0.048	2.8	8.19	10.6	1.75	0.42	26	0.95	0.75
	PME-091520	9/15/20	1.00	19.5	1.3 (0.1)	0.245	0.058	3.5	7.85	11.8	1.54	0.36	37	0.88	0.72
	PME-100820	10/8/20	0.99	33.9	2.7 (0.2)	0.441	0.090	5.4	7.58	15.1	1.25	0.26	81	0.90	0.73
Averages															
Winter & Spring (Win-Spr)				9.9 (1.5)					7.7 (0.3)	8.0 (1.0)	1.88 (0.42)	0.53 (0.15)			
Summer & Fall (Sum-Fall)				7.4 (0.4)					9.1 (0.5)	13.7 (3.1)	0.65 (0.19)	0.14 (0.05)			
Fresh wildfire (FBB)				55 (10)					7.3 (0.2)	5.8 (1.5)	3.29 (0.40)	1.16 (0.31)			
Aged wildfire (ABB)				24 (8)					7.9 (0.3)	12.5 (2.3)	1.51 (0.25)	0.35 (0.08)			

Field blanks[l]													
FB1	8/4/20	3 min	6.9	0.16 (0.06)	0.0022	0.0004	0.017				0	2.12	1	
FB2	1/2/20	3 min	15.6	0.13 (0.06)	0.0015	0	0.0013				0.16	2.04	1	
FB3	10/5/20	3 min	39.6	0.47 (0.38)	0.0065	0.0014	0.086				0	2.98	1	

Listed uncertainties (in parentheses) are ± 1 standard deviation. Values in the table are not normalized by the sampling duration.

[a] For 24-h samples, sampling started in the morning of the first date shown and ended on the second date.

[b] Average ambient $PM_{2.5}$ concentration for each sampling period measured at the UC Davis sampling site by the California Air Resources as reported on the *i*ADAM online database (California Air Resources Board, 2019-2020).

[c] Average particle mass/water mass ratio (± 1σ) in each extract, calculated as the extracted particle mass per square (determined as the difference of filter weights before and after extraction) divided by the mass of water used to extract the square. Each value is an upper bound because the measured mass of PM extracted includes insoluble material that would be removed by the subsequent filtration step.

[d] Base-10 absorption coefficient of the extract (in cm^{-1}) at 300 nm.

[e] Base-10 absorption coefficient of the extract (in cm^{-1}) at 365 nm.

[f] Rate of sunlight absorption by PME between 300 and 450 nm, calculated by equation 2 in Kaur et al. (2019), using midday actinic flux on the winter solstice in Davis (photons cm^{-2} s^{-1} nm^{-1}) from the Tropospheric Ultraviolet and Visible (TUV) Radiation Model version 4.1.

[g] AAE (Ångstrom Absorption Exponent) is calculated as the negative slope of a linear regression between ln(absorbance) vs. ln(wavelength) in the 300 – 450 nm wavelength range.

[h] The ratio of absorbance at 250 nm divided by absorbance at 365 nm.

[i] Mass absorption coefficient at 300 or 365 nm normalized by dissolved organic carbon, calculated as $MAC_{DOC,\lambda} = \frac{\alpha_\lambda \times \ln(10) \times 10^6}{[DOC]}$ (Kaur et al., 2019). The nitrate and nitrite contributions to absorbance at each wavelength were subtracted but were very small, < 5 % of total absorbance at either wavelength.

[j] Light-absorption-weighted internal screening factor, calculated with equation 2 in Smith et al. (2016), using the midday winter solstice actinic flux in Davis. The wavelength range used is 280-364 nm. A value of 1 indicates no light screening while a low value represents a strong screening effect. The "PME" column shows light screening factors in PME samples, while the "PME+DMB" column shows values in the PME with added 80 µM DMB (which was used for inhibition factor measurements; see Section S1). The cell pathlength was 0.5 cm.

[k] These two samples are the interpolations of the winter and summer samples, respectively, from our previous work on the dependence of photooxidant concentration on dilution (Ma et al., 2023a). Their particle mass/water mass ratios, absorbances, and DOC values were estimated for an equivalent extraction volume of 1.0 mL water/square by interpolating from the winter or summer linear trend for each variable as a function of concentration factor.

[l] Field blank filters were obtained using the same procedure as for samples, by loading clean filters into the sampler and turning on the pump for 3 min. Field blank samples were extracted with 1.0 mL water/square.

Table S2. Ion concentrations in PMEs

Sample Type	Sample ID	Sampling duration (days)	$[NO_3^-]$ (µM)	$[NO_2^-]$ (µM)	$[SO_4^{2-}]$ (µM)[a]	$[Cl^-]$ (µM)	$[HCOO^-]$ (µM)	$[NH_4^+]$ (µM)	$[Na^+]$ (µM)	$[K^+]$ (µM)	$[Ca^{2+}]$ (µM)
Winter & Spring	PME-111519	7.00	2660	8.98	838	811[b]	76.4	4857	718	1187[b]	373
	PME-120319	1.00	541	0.87	39.6	17.4	3.5	653	151	79.1	28.0
	PME-122019	7.01	3309	2.65	296	167[b]	61.0	2198	246	84.7[b]	70.1
	PME-010220	1.01	424	0.69	25.2	10.7	3.4	516	147	64.7	28.0
	PME-010620	7.01	3075	3.14	400	750[b]	56.0	1620	183	272[b]	141
	PME-021620[e]	7.07	1480	6.08	617	37.3	51.5	1300	1159	214	402
	PME-022020	1.00	84.0	0.81	58.0	0.3	3.8	168	165	61.8	28.1
	PME-030420	1.01	356	0.75	65.2	66.7	18.2	99.4	138	26.3	28.0
Summer & Fall	PME-070720	0.99	117	0.63	69.5	238	5.8	65.5	548	36.9	187
	PME-080420	1.01	90.0	0.50	87.1	1654[b]	10.3	78.7	457	1559[b]	143
	PME-101520	1.00	25.5	0.44	-9.1	17.1	0.5	58.5	240	22.7	28.0
Fresh wildfire	PME-081920	0.99	288	1.88	76.3	72.3	81.6	46.2	127	122	200
	PME-082220[e]	1.20	299	2.50	173	51.8	64.2	460	529	219	233
	PME-082420	0.92	179	1.72	157	516[b]	32.9	502	292	676[b]	184
	PME-090920	1.00	219	1.42	82.9	23.7	69.3	66.3	109	64.3	210
Aged wildfire	PME-090120	0.99	180	0.75	99.1	64.1	14.6	65.8	538	53.8	193
	PME-091520	1.00	66.1	0.63	29.8	0.5	< LOD[d]	112	195	55.3	111
	PME-100820	0.99	204	1.26	83.0	1164[b]	20.8	803	300	1310[b]	137
Field blanks											
	FB1[c]	3 min	3.12	<LOD[d]	< 0	2458	3.03	0.12	96.0	ND[f]	7.01
	FB2	3 min	4.58	<LOD[d]	< 0	1.07	2.94	1.42	93.8	5.92	7.02
	FB3	3 min	1.99	<LOD[d]	12.4	0.65	5.54	1.11	124.6	8.88	7.08

Values in the table are not normalized by the sampling duration.

[a] The amount of added sulfuric acid for pH adjustment (typically 90 µM) has been subtracted.

[b] These samples were contaminated by pH electrode filling solution (potassium chloride) during pH adjustment. These samples are not included in the discussion of K^+ concentrations in the main text.

[c] This field blank sample was contaminated by the pH electrode filling solution, resulting in an extremely high Cl^- concentration.

[d] Below limit of detection.

[e] These two samples are the interpolations of the winter and summer samples, respectively, from our previous work on the dependence of photooxidant concentration on dilution (Ma et al., 2023a). Their ion concentration values were estimated by interpolation from the winter or summer linear trend for each variable with concentration factor to an equivalent extraction volume of 1.0 mL water/square.

[f] Not determined due to the poor ion chromatogram result.
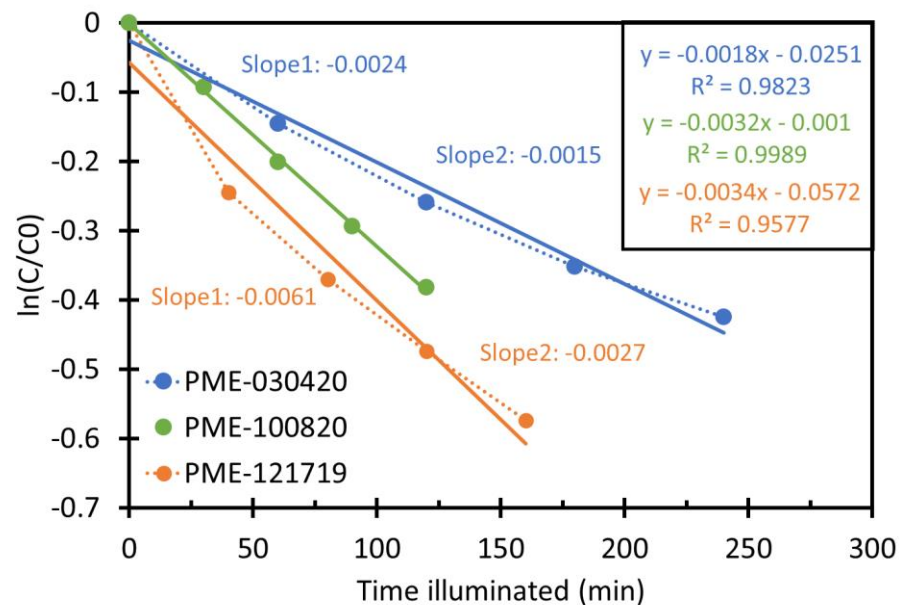
Figure S1. Representative plots of benzoic acid decay kinetics in aqueous particle extracts showing samples where: (1) the initial rate of BA loss is roughly twice as fast as the later rate (orange), (2) the initial rate is roughly 50% higher than the later rate (blue) and (3) there is no difference in BA decay over the course of illumination (green). Solid lines are linear regressions to all points for a given sample, while their regression equations are shown in the right top box. For the orange and blue data, Slope 1 and Slope 2 represent slopes from linear regressions of the first two and last four data points, respectively.

Table S3. Hydroxyl radical measurements

Sample Type	Sample ID	P_{OH} (10^{-9} $M^{-1}s^{-1}$)[a]	k'_{OH} (10^6 s^{-1})[b]	[•OH][c] (10^{-15} M) from BA	[•OH][d] (10^{-15} M) from p-HBA	Average [•OH] (10^{-15} M)[e]	$10^{-4} \times \Phi_{OH}$[f]	%$P_{OH,NO3^-}$[g]	%$P_{OH,NO2^-}$[h]
Winter & Spring	PME-111519	14 (2)	4.3 (0.6)	2.4 (0.3)	3.9 (0.5)	3.2 (0.3)	5.4 (0.9)	2.7 (0.4)	1.7 (0.3)
	PME-120319	0.44 (0.06)	0.36 (0.05)	1.4 (0.1)	1.1 (0.1)	1.2 (0.1)	2.7 (0.4)	17 (2)	5.1 (0.7)
	PME-122019	6.0 (0.9)	1.6 (0.2)	3.0 (0.4)	4.8 (0.5)	3.9 (0.3)	5.1 (0.8)	7.7 (1.2)	1.1 (0.2)
	PME-010220	0.60 (0.08)	0.38 (0.05)	1.6 (0.1)	1.5 (0.1)	1.6 (0.1)	3.3 (0.4)	9.9 (1.3)	3.0 (0.4)
	PME-010620	6.7 (1.0)	1.4 (0.2)	3.5 (0.3)	5.8 (0.5)	4.7 (0.3)	7.9 (1.1)	6.5 (0.9)	1.2 (0.2)
	PME-021620[i]	10 (2)	2.1 (0.3)			4.7 (0.4)	6.3 (0.1)	2.1 (0.4)	1.6 (0.2)
	PME-022020	0.45 (0.06)	0.48 (0.06)	1.1 (0.1)	0.83 (0.1)	0.94 (0.05)	1.1 (0.2)	2.6 (0.4)	4.7 (0.7)
	PME-030420	0.52 (0.08)	0.36 (0.05)	1.4 (0.1)	1.5 (0.2)	1.5 (0.1)	4.0 (0.6)	9.5 (1.4)	3.7 (0.6)
Summer & Fall	PME-070720	0.20 (0.03)	0.26 (0.03)	0.90 (0.03)	0.59 (0.1)	0.74 (0.05)	3.9 (0.6)	8.4 (1.2)	8.4 (1.2)
	PME-080420	0.050 (0.026)	0.22 (0.03)		0.23 (0.03)	0.23 (0.03)	2.3 (0.4)	25 (13)	26 (13)
	PME-101520	0.038 (0.015)	0.11 (0.01)	0.28 (0.19)	0.30 (0.15)	0.34 (0.12)	1.6 (0.6)	9.2 (3.5)	30 (11)
Fresh wildfire	PME-081920	7.3 (1.3)	2.7 (0.3)	2.6 (0.5)	2.9 (0.4)	2.8 (0.3)	1.7 (0.3)	0.55 (0.10)	0.67 (0.12)
	PME-082220[i]	8.7 (1.3)	3.4 (0.4)			2.6 (0.2)	2.3 (0.3)	0.48 (0.07)	0.75 (0.11)
	PME-082420	4.8 (1.2)	2.4 (0.3)	2.1 (0.2)	1.9 (0.9)	2.0 (0.4)	1.7 (0.3)	0.52 (0.13)	0.93 (0.24)
	PME-090920	4.2 (0.9)	1.6 (0.2)	2.0 (0.1)	3.4 (0.9)	2.7 (0.5)	2.8 (0.3)	0.73 (0.16)	0.88 (0.19)
Aged wildfire	PME-090120	0.28 (0.04)	0.59 (0.08)	0.43 (0.01)	0.53 (0.1)	0.48 (0.03)	1.0 (0.1)	9.0 (1.3)	7.0 (1.0)
	PME-091520	1.1 (0.1)	0.82 (0.11)	1.6 (0.01)	1.2 (0.1)	1.4 (0.1)	3.2 (0.4)	0.82 (0.11)	1.4 (0.2)
	PME-100820	5.7 (0.8)	1.8 (0.2)	3.0 (0.2)	3.3 (0.2)	3.2 (0.2)	10 (1.5)	0.50 (0.07)	0.57 (0.08)
Averages[j]									
Winter & Spring						1.5 (0.3)	4.5 (2.2)	7.2 (5.0)	2.8 (1.6)
Summer & Fall						0.41 (0.03)	2.8 (1.0)	7.1 (6.5)	17 (22)
Fresh wildfire						2.5 (0.3)	2.1 (0.5)	0.57 (0.11)	0.81 (0.12)
Aged wildfire						1.7 (1.4)	4.9 (5.0)	3.4 (4.8)	3.0 (3.5)
Field Blanks									
FB1						0.57 (0.03)			
FB2[k]	0.0011 (0.0001)	0.20 (0.02)			0.06 (0.01)		5.7 (0.5)	36 (3)
FB3[k]	0.0008 (0.0001)	0.05 (0.02)			0.15 (0.01)		3.6 (0.4)	26 (3)

Listed uncertainties (in parentheses) are ± 1 standard error from the errors in regressions, except for the averages, which are ± 1σ. Values in the table are not normalized by the sampling duration, but the average [•OH] was calculated after normalizing 7-day concentrations to 1 day.

[a] Davis winter solstice-normalized rate of •OH photoproduction, calculated as $P_{OH} = k'_{OH} \times$ [•OH].

[b] Apparent pseudo-first-order rate constant for destruction of •OH due to natural sinks, estimated as $k'_{OH} = k_{OH+DOC} \times$ [DOC], where k_{OH+DOC} is (2.7 (±0.4) $\times 10^8$ L (mol C)$^{-1}$ s^{-1}), the average second-order rate constant of DOC reacting with •OH from the samples in Ma et al. (2023a).

[c] Winter solstice-normalized steady-state concentration of $^\bullet$OH determined from BA decay.

[d] Winter solstice-normalized steady-state concentration of $^\bullet$OH determined from p-HBA formation.

[e] Average of concentrations of $^\bullet$OH determined by BA and p-HBA. For PME-080420 with a poor BA decay, only the value from p-HBA is used.

[f] Apparent quantum yield of $^\bullet$OH during simulated sunlight illumination, calculated as $\Phi_{OH} = P_{OH}/R_{abs.}$

[g] Percentage of $^\bullet$OH photoproduction due to nitrate photolysis. This was calculated as $(j_{NO3\text{-}\to OH} \times [NO_3^-])/P_{OH}$, using an aqueous nitrate photolysis rate constant, $j_{NO3\to OH} = 1.4 \times 10^{-7}$ s^{-1} (Anastasio and McGregor, 2001) and the measured molar concentration of NO_3^-.

[h] Percentage of $^\bullet$OH photoproduction due to of nitrite photolysis. This was calculated as $(j_{NO2\text{-}\to OH} \times [NO_2^-])/P_{OH}$, using an aqueous nitrite photolysis rate constant, $j_{NO2\to OH} = 2.6 \times 10^{-5}$ s^{-1} (Anastasio and McGregor, 2001) and the measured molar concentration of NO_2^-.

[i] These two samples are the interpolated winter and summer samples, respectively, from our previous work on the dependence of photooxidant concentration on dilution (Ma et al., 2023a). The $^\bullet$OH concentration in PME-021620 was the average concentration of the winter dilution series because their concentration is independent of concentration factor. The $^\bullet$OH concentration in PME-081920 was estimated by interpolating the linear trends between [$^\bullet$OH] and concentration factor in the summer dilution series to an equivalent extraction volume of 1 mL water/square.

[j] The average value of each sample type. For the average [$^\bullet$OH] calculation, the $^\bullet$OH concentration normalized by sampling duration is used.

[k] The $^\bullet$OH production rate in field blanks was determined by adding 1.2 mM benzoic acid to 1.0 mL FB sample and monitoring the formation of p-hydroxy benzoic acid, assuming that all $^\bullet$OH produced reacts with benzoic acid.

Table S4. Singlet molecular oxygen measurements

Sample Type	Sample ID	$[^1O_2^*]^a$ $(10^{-12}$ M)	$P_{1O2^*}^b$ $(10^{-7}$ M s$^{-1})$	$f_{FFA,1O2^*}{}^c$	$f_{FFA,OH}{}^d$	$10^2 \times$ $\Phi_{1O2^*}{}^e$	$\Phi_{3C^*,SYR}/$ $(\Phi_{1O2^*}/f_\Delta)^f$	$\Phi_{3C^*,PTA}/$ $(\Phi_{1O2^*}/f_\Delta)^g$	$[^3C^*]_{SYR}/[^1O_2^*]^h$	$[^3C^*]_{PTA}/[^1O_2^*]^i$
Winter & Spring	PME-111519	4.5 (0.4)	9.9 (1.0)	0.85 (0.09)	0.17 (0.02)	4.0 (0.4)	0.81 (0.23)	0.45 (0.12)	0.17 (0.05)	0.10 (0.03)
	PME-120319	0.37 (0.07)	0.81 (0.16)	0.73 (0.15)	0.35 (0.01)	5.0 (1.0)	0.28 (0.08)	0.21 (0.07)	0.13 (0.04)	0.10 (0.03)
	PME-122019	2.5 (0.2)	5.5 (0.4)	0.76 (0.07)	0.37 (0.03)	4.6 (0.4)	0.52 (0.16)	0.24 (0.06)	0.18 (0.06)	0.08 (0.02)
	PME-010220	0.27 (0.06)	0.59 (0.12)	0.51 (0.11)	0.83 (0.04)	3.2 (0.7)	0.28 (0.09)	0.32 (0.10)	0.13 (0.04)	0.15 (0.05)
	PME-010620	2.3 (0.2)	5.1 (0.4)	0.81 (0.07)	0.47 (0.03)	6.0 (0.5)	0.24 (0.05)	0.26 (0.07)	0.08 (0.02)	0.09 (0.02)
	PME-021620^j	1.9 (0.3)	4.2 (0.7)			2.7 (0.4)	0.58 (0.18)	0.38 (0.11)	0.18 (0.06)	0.11 (0.03)
	PME-022020	0.59 (0.06)	1.3 (0.1)	0.92 (0.11)	0.42 (0.02)	3.2 (0.3)	0.42 (0.09)	0.21 (0.06)	0.19 (0.04)	0.10 (0.03)
	PME-030420	0.20 (0.03)	0.44 (0.06)	0.52 (0.07)	1.03 (0.07)	3.4 (0.5)	0.14 (0.05)	0.24 (0.07)	0.07 (0.02)	0.11 (0.03)
Summer & Fall	PME-070720	0.17 (0.02)	0.38 (0.04)	1.01 (0.11)	1.23 (0.08)	7.5 (0.7)	0.29 (0.06)	0.10 (0.03)	0.14 (0.03)	0.05 (0.01)
	PME-080420	0.081 (0.027)	0.18 (0.06)	0.97 (0.33)	0.78 (0.39)	7.9 (2.7)	0.22 (0.09)	0.07 (0.04)	0.11 (0.04)	0.04 (0.02)
	PME-101520	0.068 (0.006)	0.15 (0.01)	1.46 (0.31)	0.82 (0.30)	8.4 (0.8)	0.54 (0.11)	0.15 (0.05)	0.28 (0.06)	0.08 (0.02)
Fresh wildfire	PME-081920	3.3 (0.6)	7.2 (1.2)	1.13 (0.22)	0.26 (0.03)	1.7 (0.3)	0.44 (0.12)	0.20 (0.07)	0.12 (0.03)	0.06 (0.02)
	PME-082220^j	3.8 (1.0)	8.4 (2.1)			2.2 (0.6)	0.54 (0.18)	0.20 (0.07)	0.13 (0.05)	0.05 (0.02)
	PME-082420	3.0 (0.2)	6.7 (0.5)	0.80 (0.06)	0.02 (0.01)	2.3 (0.2)	0.71 (0.19)	0.19 (0.05)	0.21 (0.06)	0.06 (0.01)
	PME-090920	1.9 (0.2)	4.2 (0.5)	0.73 (0.09)	0.15 (0.03)	2.8 (0.3)	0.59 (0.34)	0.29 (0.19)	0.21 (0.12)	0.10 (0.06)
Aged wildfire	PME-090120	0.45 (0.06)	0.99 (0.12)	0.65 (0.09)	0.20 (0.01)	3.5 (0.4)	0.78 (0.19)	0.26 (0.07)	0.34 (0.08)	0.12 (0.03)
	PME-091520	0.50 (0.04)	1.1 (0.1)	0.56 (0.05)	0.44 (0.02)	3.2 (0.2)	0.63 (0.15)	0.27 (0.07)	0.26 (0.06)	0.11 (0.03)
	PME-100820	1.2 (0.2)	2.7 (0.4)	0.98 (0.13)	0.71 (0.04)	5.0 (0.7)	0.45 (0.10)	0.16 (0.04)	0.15 (0.03)	0.05 (0.01)
Averages^k										
Winter & Spring		0.38 (0.16)				4.0 (1.1)	0.41 (0.22)	0.29 (0.09)	0.14 (0.05)	0.11 (0.02)
Summer & Fall		0.11 (0.06)				7.9 (0.4)	0.35 (0.17)	0.11 (0.04)	0.17 (0.09)	0.05 (0.02)
Fresh wildfire		2.9 (0.7)				2.2 (0.5)	0.57 (0.11)	0.22 (0.04)	0.17 (0.05)	0.07 (0.02)
Aged wildfire		0.73 (0.44)				3.9 (1.0)	0.62 (0.17)	0.23 (0.06)	0.25 (0.10)	0.09 (0.04)
Field blanks										
FB1		0.016 (±0.001)		0.81 (±0.15)	8.3 (±4.8)					
FB2		0.021 (±0.001)		0.66 (±0.33)	0.54 (±0.07)					
FB3		0.028 (±0.001)		0.97 (±0.17)	0.73 (±0.09)					

Listed uncertainties (in parentheses) are ± 1 standard error propagated from the errors in regressions and rate constants, except for the averages, where uncertainties are ± 1σ. Values in the table are not normalized by the sampling duration, but the average $[^1O_2^*]$ was calculated using 7-day concentrations normalized to 1 day.

[a] Davis winter solstice-normalized steady-state concentration of $^1O_2^*$.

[b] Production rate of $^1O_2^*$, calculated as $P_{1O2^*} = [^1O_2^*] \times k'_{H2O}$, where k'_{H2O} is the first-order rate constant for loss of $^1O_2^*$ in H_2O (2.2×10^5 s^{-1}) (Bilski et al., 1997).

[c] Fraction of FFA lost due to $^1O_2^*$ in PME diluted with H_2O (i.e., 0.5 mL PME + 0.5 mL H_2O), calculated as $f_{FFA,1O2*} = [^1O_2^*]/2 \times k_{FFA+1O2*}/k'_{FFA,H2O}$, where $k_{FFA+1O2*}$ is the second-order rate constant of FFA reacting with $^1O_2^*$, and $k'_{FFA,H2O}$ is the normalized first-order decay rate of FFA in the PME diluted with H_2O.

[d] Fraction of FFA lost due to $^\bullet OH$ in PME diluted with H_2O, estimated as $f_{FFA,OH} = [^\bullet OH] \times k_{FFA+OH}/k'_{FFA,H2O}$, where k_{FFA+OH} is the second-order rate constant of FFA reacting with $^\bullet OH$ (1.5×10^{10} M^{-1} s^{-1}) (Ross and Ross, 1977), assuming $^\bullet OH$ concentration is the same in the diluted and undiluted PME.

[e] Apparent quantum yield of $^1O_2^*$, calculated as $\Phi_{1O2*} = P_{1O2*}/R_{abs}$.

[f] Fraction of oxidizing triplets determined by SYR to the total triplet pool (Kaur and Anastasio, 2018). f_Δ is the yield of $^1O_2^*$ from oxygen quenching of triplet states, assumed to be 0.53 (McNeill and Canonica, 2016). $\Phi_{3C*,SYR}$ is the apparent quantum yield of $^3C^*$ determined by SYR (See Table S7).

[g] Fraction of oxidizing triplets determined by PTA to the total triplet pool.

[h] Ratio of triplet concentration determined by SYR to the singlet oxygen concentration.

[i] Ratio of triplet concentration determined by PTA to the singlet oxygen concentration.

[j] These two samples are the interpolated winter and summer samples, respectively, from Ma et al. (2023a). $^1O_2^*$ concentrations were estimated by interpolating the linear trends between $[^1O_2^*]$ and concentration factor in PME-10, PME-2, and PME-0.7 samples, to an equivalent extraction volume of 1 mL water/square.

[k] Average value of each sample type. The $^1O_2^*$ concentration normalized by sampling duration was used for calculating average $^1O_2^*$ concentrations.

Table S5. Rate constants of SYR and PTA reacting with triplet excited states, singlet oxygen, and hydroxyl radical at pH 4.2

Oxidants	k_{SYR+Ox} (M^{-1} s^{-1})	Reference	k_{PTA+Ox} (M^{-1} s^{-1})	Reference
$^{\bullet}$OH	20 ($\pm$4) $\times$ 10^9	(Smith et al., 2015)	10.3 ($\pm$0.6) $\times$ 10^9	
^{1}O$_2$*	3.6 ($\pm$0.7) $\times$ 10^7	(Tratnyek and Hoigne, 1991)	8.8 ($\pm$0.6) $\times$ 10^6	(Ma et al., 2023b)
^{3}DMB*	3.9 ($\pm$0.7) $\times$ 10^9	(Smith et al., 2015)	2.5 ($\pm$0.6) $\times$10^9	
Direct photodegradation	j_{SYR} (s^{-1})		j_{PTA} (s^{-1})	
	< 4.3 $\times$ 10^{-6}	(Kaur and Anastasio, 2018)	6.2 ($\pm$0.2) $\times$ 10^{-4}	(Ma et al., 2023b)

Section S1. Determining inhibition factors and correcting $^3C^*$ concentrations

Dissolved organic matter in PME may inhibit the decay of SYR or PTA by triplets, leading to an underestimation of triplet concentration. Based on our previous research, SYR as a probe is more strongly inhibited than PTA (Ma et al., 2023b). To investigate and quantify the inhibition effect of PME on these two triplet probes, we measured inhibition factors (*IF*s) of FFA, SYR, and PTA for each sample, and used the *IF* values to correct meaasured $^3C^*$ concentrations in PME. Details of inhibition factors are described in Canonica et al. (2008), Wenk et al. (2011), and Ma et al. (2023b). To measure *IF*, we monitored the loss of 10 µM probe in three illuminated solutions for each sample: (1) in the pH 4.2 PME; (2) in pH 4.2 Milli-Q water containing 80 µM of triplet precursor 3,4-dimethoxybenzaldehyde (DMB); and (3) in the pH 4.2 PME with added 80 µM DMB. During each illumination we determined the first-order rate constant of probe decay. The inhibition factor for the probe was calculated using

$$IF_P = \frac{k'_{DMB,PME} - k'_{PME}}{k'_{DMB}} \tag{S1}$$

where $k'_{DMB,PME}$ is the first-order decay rate constant of probe in solution containing both DMB and PME, while k'_{PME} and k'_{DMB} are the probe loss rate constants in PME alone and in Milli-Q water with DMB, respectively. All *k'* values were corrected for internal light screening using screening factors (S_λ); the PME and PME+DMB values are listed in Table S1, while the light screening factor for 80 µM DMB is 0.75. An *IF* value of 1 indicates there is no DOM inhibition on probe decay, while *IF* = 0 indicates complete inhibition of probe decay. Since IF_P can also be affected by DOM suppressing the $^3DMB^*$ concentration, we use IF_{FFA} to quantify this triplet suppression (Ma et al., 2023b). To exclude the effect of triplet suppression on IF_{SYR} and IF_{PTA} (i.e., to quantify only inhibition due to probe regeneration), we use $IF_{SYR,corr}$ and $IF_{PTA,corr}$

$$IF_{P,corr} = \frac{IF_P}{IF_{FFA}} \tag{S2}$$

Theoretically, *IF* should not exceed 1, but we sometimes see this result. When *IF* is greater than 1, it suggests there is interaction between DOM in PME with DMB to form reactive species, and thus indicates no inhibition or suppression. Therefore, when IF_{FFA} or IF_P is greater than 1, we assume that $IF_{P,corr} = IF_P$ and we do not correct the $^3C^*$ concentration if $IF_{P,corr} > 1$. In addition, IF_{PTA} and IF_{SYR} values are expected to be lower than IF_{FFA} because IF_{PTA} and IF_{SYR} are affected by both the triplet suppression and probe inhibition effects, while IF_{FFA} is only impacted by triplet suppression. However, in some samples the IF_{PTA} value is greater than IF_{FFA}, which might be attributed to the large error in IF_{FFA} measurement in cases where the difference between $k'_{DMB,PME}$ and k'_{PME} is small for FFA. In this case, we

assume the IF_{FFA} value equals IF_{PTA} (since PTA is very resistant to suppression; (Ma et al., 2023b)) and use this value to calculate $IF_{P,corr}$. The determined IF and $IF_{P,corr}$ values are shown in Table S6.

The uncorrected ^{3}C* concentration is calculated with:

$$[^3C^*]_{P,uncorr} = \frac{k'_{P,3C*}}{k_{P+3DMB*}} \tag{S3}$$

35   where $k'_{P,3C*}$ is measured first-order rate constant of probe loss due to triplets and $k_{P+3DMB*}$ is the second-order rate constant of probe reacting with ^{3}DMB*. This assumes that triplets in our extracts have reactivities similar to triplet DMB, as we have found in our past work (Kaur and Anastasio, 2018; Kaur et al., 2019). However, it is possible that we are overestimating the P + ^{3}C* rate constant by using DMB as a model; this would lead to an underestimate of the oxidizing triplet concentrations (Ma et al., 2023). To

40   correct for the probe inhibition effect, [^{3}C*] is calculated using

$$[^3C^*]_P = \frac{[^3C^*]_{P,uncorr}}{IF_{P,corr}} \tag{S4}$$

As stated earlier, if $IF_{P,corr} > 1$, we do not apply a correction, i.e., we use [^{3}C*]$_{P,corr}$ = [^{3}C*]$_{P,uncorr}$ The ^{3}C* concentrations shown in the main text are the values after IF correction.

45

Table S6. Inhibition factors for FFA, SYR, and PTA

Sample Type	Sample ID	IF_{FFA}	IF_{SYR}	IF_{PTA}	$IF_{SYR,corr}$	$IF_{PTA,corr}$
Winter & Spring	PME-111519	0.60 (0.45)	0.27 (0.04)	1.06 (0.13)	0.27 (0.04)	1.06 (0.13)
	PME-120319	1.15 (0.12)	0.78 (0.04)	1.16 (0.07)	0.78 (0.04)	1.16 (0.07)
	PME-122019	1.30 (0.12)	0.21 (0.04)	1.26 (0.03)	0.21 (0.04)	1.26 (0.03)
	PME-010220	1.06 (0.10)	0.53 (0.04)	1.24 (0.04)	0.53 (0.04)	1.24 (0.04)
	PME-010620	0.97 (0.20)	0.48 (0.03)	1.24 (0.06)	0.48 (0.03)	1.24 (0.06)
	PME-021620[a]	0.62 (0.07)	0.20 (0.02)	0.87 (0.19)	0.24 (0.03)	1.00 (0.08)
	PME-022020	1.36 (0.08)	0.81 (0.05)	1.40 (0.08)	0.81 (0.05)	1.40 (0.08)
	PME-030420	1.16 (0.03)	0.58 (0.05)	1.28 (0.08)	0.58 (0.06)	1.28 (0.08)
Summer & Fall	PME-070720	1.28 (0.05)	0.76 (0.06)	1.47 (0.07)	0.76 (0.03)	1.47 (0.07)
	PME-080420	1.14 (0.07)	0.76 (0.03)	0.75 (0.02)	0.76 (0.05)	0.75 (0.02)
	PME-101520	1.03 (0.04)	1.02 (0.05)	1.15 (0.05)	1.02 (0.05)	1.15 (0.05)
Fresh wildfire	PME-081920	0.27 (0.05)	0.23 (0.01)	0.51 (0.04)	0.46 (0.05)	1.00 (0.12)
	PME-082220[a]	0.52 (0.05)	0.25 (0.02)	0.57 (0.07)	0.47 (0.05)	0.96 (0.11)
	PME-082420	1.01 (0.12)	0.31 (0.02)	0.60 (0.04)	0.31 (0.02)	0.60 (0.04)
	PME-090920	0.90 (0.47)	0.88 (0.03)	0.79 (0.03)	0.98 (0.51)	0.88 (0.52)
Aged wildfire	PME-090120	1.18 (0.12)	0.85 (0.09)	0.98 (0.04)	0.85 (0.09)	0.98 (0.04)
	PME-091520	0.95 (0.04)	0.82 (0.11)	0.87 (0.04)	0.87 (0.12)	0.92 (0.06)
	PME-100820	1.18 (0.09)	1.19 (0.15)	1.32 (0.10)	1.19 (0.15)	1.32 (0.10)
Averages						
Winter & Spring					0.49 (0.23)	1.20 (0.13)
Summer & Fall					0.85 (0.15)	1.12 (0.36)
Fresh wildfire					0.55 (0.29)	0.86 (0.18)
Aged wildfire					0.97 (0.19)	1.07 (0.22)
Field blanks						
FB1		0.95 (±0.12)	0.52 (±0.05)[b]	0.86 (±0.13)	0.54 (±0.08)[b]	0.90 (±0.19)
FB2		1.10 (±0.05)	0.95 (±0.19)	0.93 (±0.06)	0.95 (±0.19)	0.93 (±0.06)
FB3		1.21 (±0.06)	1.20 (±0.08)	1.15 (±0.09)	1.20 (±0.08)	1.15 (±0.09)

Listed uncertainties (in parentheses) are ± 1 standard error propagated from the errors in data regression, except for the averages (± 1σ)

[a] These two samples are interpolated from the winter and summer samples, respectively, in Ma et al. (2023a). IF values were estimated by interpolating the linear regression between 1/IF for each probe vs. concentration factor, to an equivalent extraction volume of 1 mL water/square.

[b] The low IF_{SYR} might be attributed to the contamination of this field blank by pH electrode filling solution.

Table S7. Oxidizing triplet excited state measurements by syringol (SYR)

Sample Type	Sample ID	k'_{SYR}[a] (10^{-4} s^{-1})	$f_{SYR,OH}$[b]	$f_{SYR,1O2*}$[c]	$f_{SYR,3C*}$[d]	$[^3C^*]_{SYR,uncorr}$[e] (10^{-14} M)	$[^3C^*]_{SYR}$[f] (10^{-14} M)	$k'_{3C*,SYR}$[g] (10^6 s^{-1})	$P_{3C*,SYR}$[h] (10^{-7} M s^{-1})	$\Phi_{3C*,SYR}$[i] (%)
Winter & Spring	PME-111519	11 (0.7)	0.06 (0.01)	0.15 (0.04)	0.79 (0.09)	22 (4)	79 (21)	1.9	15 (4)	6.0 (1.6)
	PME-120319	1.9 (0.1)	0.14 (0.03)	0.07 (0.02)	0.79 (0.10)	3.8 (0.8)	4.9 (1.0)	0.88	0.43 (0.09)	2.6 (0.6)
	PME-122019	5.3 (0.5)	0.15 (0.03)	0.17 (0.04)	0.69 (0.12)	9.4 (2.2)	45 (13)	1.2	5.4 (1.6)	4.6 (1.4)
	PME-010220	1.1 (0.1)	0.29 (0.06)	0.09 (0.03)	0.63 (0.11)	1.8 (0.4)	3.4 (0.9)	0.88	0.31 (0.08)	1.7 (0.4)
	PME-010620	5.4 (0.2)	0.17 (0.04)	0.15 (0.03)	0.67 (0.06)	9.3 (1.9)	19 (4)	1.2	2.3 (0.5)	2.7 (0.6)
	PME-021620[j]						35 (9)	1.4	4.7 (1.3)	2.9 (0.8)
	PME-022020	3.9 (0.2)	0.05 (0.01)	0.05 (0.01)	0.90 (0.05)	9.0 (1.7)	11 (2)	0.91	1.0 (0.2)	2.5 (0.5)
	PME-030420	0.66 (0.04)	0.44 (0.10)	0.11 (0.03)	0.45 (0.12)	0.77 (0.24)	1.3 (0.4)	0.88	0.12 (0.04)	0.9 (0.3)
Summer & Fall	PME-070720	0.91 (0.2)	0.16 (0.03)	0.07 (0.01)	0.77 (0.05)	1.8 (0.3)	2.4 (0.5)	0.85	0.20 (0.04)	4.0 (0.8)
	PME-080420	0.33 (0.03)	0.14 (0.08)	0.09 (0.04)	0.77 (0.13)	0.66 (0.15)	0.87 (0.21)	0.84	0.073 (0.017)	3.3 (0.8)
	PME-101520	0.81 (0.02)	0.08 (0.03)	0.03 (0.01)	0.89 (0.05)	1.9 (0.3)	1.9 (0.3)	0.81	0.15 (0.03)	8.5 (1.6)
Fresh wildfire	PME-081920	8.8 (0.1)	0.06 (0.01)	0.13 (0.03)	0.80 (0.04)	18.3 (3.5)	40 (9)	1.5	5.9 (1.3)	1.4 (0.3)
	PME-082220[j]						51 (12)	1.7	8.6 (2.0)	2.2 (0.5)
	PME-082420	9.2 (1.2)	0.04 (0.01)	0.12 (0.03)	0.84 (0.18)	20 (5)	64 (16)	1.4	9.0 (2.3)	3.1 (0.8)
	PME-090920	16 (4)	0.03 (0.01)	0.04 (0.01)	0.92 (0.04)	39 (7)	40 (22)	1.2	4.8 (2.6)	3.1 (1.7)
Aged wildfire	PME-090120	5.3 (0.1)	0.02 (0.01)	0.03 (0.01)	0.95 (0.04)	13 (8)	15 (3)	0.94	1.5 (0.3)	5.2 (1.1)
	PME-091520	4.8 (0.1)	0.06 (0.01)	0.04 (0.01)	0.91 (0.03)	11 (2)	13 (3)	1.0	1.3 (0.3)	3.8 (0.9)
	PME-100820	8.0 (0.3)	0.08 (0.02)	0.06 (0.01)	0.87 (0.05)	18 (3)	18 (3)	1.3	2.3 (0.4)	4.2 (0.8)
Averages[k]										
Winter & Spring							5.8 (3.7)			3.3 (1.6)
Summer & Fall							1.2 (0.78)			5.3 (2.8)
Fresh wildfire							48 (14)			2.5 (0.8)
Aged wildfire							16 (2.5)			4.4 (0.7)
Field blanks										
FB1		0.052 (±0.004)	2.20 (±1.34)	0.11 (±0.02)	-1.31 (±1.34)	-0.018 (±0.018)	-0.32 (±0.33)			
FB2		0.13 (±0.01)	0.09 (±0.02)	0.05 (±0.01)	0.86 (±0.03)	0.30 (±0.05)	0.32 (±0.08)			
FB3		0.20 (±0.01)	0.15 (±0.04)	0.05 (±0.01)	0.80 (±0.06)	0.42 (±0.08)	0.42 (±0.08)			

Listed uncertainties (in parentheses) are ± 1 standard error propagated from the errors in the regression and rate constants, except for the averages, which are ± 1σ. Values in the table are not normalized by the sampling duration, but the average triplet concentrations are calculated using 7-day concentrations normalized to 1-day equivalent values.

[a] Davis winter-solstice-normalized pseudo-first-order rate constant for loss of syringol (SYR)

[b] Fraction of SYR loss due to hydroxyl radical, calculated as $f_{SYR,OH} = (k_{SYR+OH} \times [^{\bullet}OH])/k'_{SYR}$

[c] Fraction of SYR loss due to singlet oxygen, calculated as $f_{SYR,1O2*} = (k_{SYR+1O2*} \times [^1O_2^*])/k'_{SYR}$.

[d] Fraction of SYR loss due to triplets, calculated as $f_{SYR,3C*} = (1 - f_{SYR,OH} - f_{SYR,1O2*})$.

Table S8. Oxidizing triplet excited state measurements by (phenylthio)acetic acid (PTA)

Sample Type	Sample ID	k'_{PTA} [a] (10^{-4} s^{-1})	$f_{PTA,OH}$ [b]	$f_{PTA,1O2*}$ [c]	$f_{PTA,3C*}$ [d]	$[^3C^*]_{PTA,uncorr}$ [e] (10^{-14} M)	$[^3C^*]_{PTA}$ [f] (10^{-14} M)	$k'_{3C*,PTA}$ [g] (10^6 s^{-1})	$P_{3C*,PTA}$ [h] (10^{-7} M s^{-1})	$\Phi_{3C*,PTA}$ [i] (%)	$[^3C^*]_{PTA}/[^3C^*]_{SYR}$ [j]
Winter & Spring	PME-111519	12 (1)	0.03 (0.01)	0.03 (0.01)	0.94 (0.06)	44 (11)	44 (11)	2.0	8.5 (2.1)	3.4 (0.8)	0.55 (0.20)
	PME-120319	1.1 (0.1)	0.12 (0.01)	0.03 (0.01)	0.85 (0.02)	3.6 (0.9)	3.6 (0.9)	0.88	0.32 (0.08)	2.0 (0.5)	0.75 (0.24)
	PME-122019	5.7 (0.1)	0.07 (0.01)	0.04 (0.01)	0.89 (0.01)	20 (5)	20 (5)	1.2	2.4 (0.6)	2.1 (0.5)	0.45 (0.17)
	PME-010220	1.2 (0.1)	0.14 (0.01)	0.02 (0.01)	0.84 (0.02)	4.0 (1.0)	4.0 (1.0)	0.89	0.35 (0.08)	1.9 (0.5)	1.2 (0.4)
	PME-010620	5.9 (0.1)	0.08 (0.01)	0.03 (0.01)	0.89 (0.03)	21 (5)	21 (5)	1.2	2.5 (0.6)	2.9 (0.7)	1.1 (0.4)
	PME-021620[k]						22 (6)	1.4	3.0 (0.8)	1.9 (0.5)	0.64 (0.24)
	PME-022020	1.6 (0.1)	0.06 (0.02)	0.03 (0.01)	0.90 (0.08)	5.7 (1.4)	5.7 (1.4)	0.91	0.52 (0.13)	1.3 (0.3)	0.51 (0.16)
	PME-030420	0.74 (0.06)	0.20 (0.02)	0.02 (0.01)	0.77 (0.07)	2.3 (0.6)	2.3 (0.6)	0.88	0.20 (0.05)	1.5 (0.4)	1.7 (0.7)
Summer & Fall	PME-070720	0.31 (0.01)	0.25 (0.02)	0.05 (0.01)	0.70 (0.04)	0.85 (0.21)	0.85 (0.21)	0.86	0.073 (0.018)	1.4 (0.4)	0.36 (0.11)
	PME-080420	0.084 (0.014)	0.28 (0.15)	0.08 (0.03)	0.64 (0.25)	0.21 (0.09)	0.28 (0.12)	0.84	0.024 (0.010)	1.1 (0.5)	0.33 (0.16)
	PME-101520	0.17 (0.02)	0.21 (0.08)	0.03 (0.01)	0.76 (0.14)	0.52 (0.15)	0.52 (0.15)	0.81	0.042 (0.012)	2.4 (0.7)	0.28 (0.10)
Fresh wildfire	PME-081920	5.2 (0.1)	0.05 (0.01)	0.06 (0.01)	0.89 (0.03)	18 (4)	18 (4)	1.5	2.8 (0.8)	0.64 (0.17)	0.46 (0.16)
	PME-082220[k]						19 (5)	1.7	3.2 (0.9)	0.84 (0.23)	0.37 (0.13)
	PME-082420	3.0 (0.2)	0.07 (0.02)	0.09 (0.01)	0.84 (0.07)	10 (3)	17 (4)	1.4	2.4 (0.6)	0.85 (0.22)	0.27 (0.10)
	PME-090920	4.6 (0.1)	0.06 (0.01)	0.04 (0.01)	0.90 (0.04)	17 (4)	19 (12)	1.2	2.3 (1.5)	1.5 (1.0)	0.48 (0.41)
Aged wildfire	PME-090120	1.4 (0.1)	0.04 (0.01)	0.03 (0.01)	0.94 (0.03)	5.1 (1.2)	5.2 (1.3)	0.94	0.49 (0.12)	1.8 (0.4)	0.34 (0.11)
	PME-091520	1.5 (0.1)	0.10 (0.01)	0.03 (0.01)	0.87 (0.04)	5.1 (1.2)	5.5 (1.4)	1.0	0.56 (0.14)	1.6 (0.4)	0.42 (0.14)
	PME-100820	2.1 (0.1)	0.16 (0.01)	0.05 (0.01)	0.79 (0.03)	6.5 (1.6)	6.5 (1.6)	1.3	0.83 (0.20)	1.5 (0.4)	0.36 (0.11)
Averages[m]											
Winter & Spring							3.9 (1.4)			2.1 (0.7)	0.86 (0.43)
Summer & Fall							0.57 (0.29)			1.6 (0.7)	0.32 (0.04)
Fresh wildfire							18 (0.16)			0.96 (0.39)	0.39 (0.10)
Aged wildfire							5.7 (0.7)			1.6 (0.1)	0.37 (0.05)
Field blanks											
FB1[l]		4.6 (±0.6)	0.01 (±0.01)	0.00 (±0.01)	0.99 (±0.14)	18.1 (±5.0)	20.1 (±7.0)				
FB2		0.028 (±0.009)	0.22 (±0.03)	0.07 (±0.01)	0.71 (±0.32)	0.078 (±0.040)	0.084 (±0.043)				
FB3		0.051 (±0.019)	0.31 (±0.04)	0.05 (±0.01)	0.64 (±0.38)	0.13 (±0.08)	0.13 (±0.08)				

80   Listed uncertainties (in parentheses) are ± 1 standard error propagated from the errors in the regression and rate constants, except for the averages, which are ± 1σ. Values in the table are not normalized by the sampling duration, but the average triplet concentration was calculated using 7-day concentrations normalized to 1-day equivalent values.

[a] Davis winter-solstice-normalized value of the measured pseudo-first-order rate constant for loss of PTA. Contribution from PTA direct photodegradation was subtracted. The PTA direct photodegradation accounted for (0.9-55) % of PTA total decay in PME samples, with an average of 11 ($\pm$ 15) % and for (2-79) % of PTA total decay in field blanks.

[b] Fraction of hydroxyl radical contribution to the loss of PTA, calculated as $f_{PTA,OH} = (k_{PTA+OH} \times [^\bullet OH])/k'_{PTA}$

[c] Fraction of singlet oxygen contribution to the loss of PTA, calculated as $f_{PTA,1O2*} = (k_{PTA+1O2*} \times [^1O_2*])/k'_{PTA}$.

[d] Fraction of PTA loss due to triplets, calculated as $f_{PTA,3C*} = (1 - f_{PTA,OH} - f_{PTA,1O2*})$.

[e] Uncorrected triplet steady-state concentration calculated from PTA loss as $k'_{PTA,3C*}/k_{PTA+3DMB*}$.

[f] Triplet concentration with inhibition factor correction, calculated as $[^3C*]_{PTA,uncorr}/IF_{PTA,corr}$.

[g] Apparent pseudo-first-order rate constant for quenching PTA-determined $^3C*$ by organic sinks and dissolved oxygen, calculated as $k'_{3C*,PTA} = k_{rxn+Q,3C*}[DOC] + k_{3C*+O2}[O_2]$, where $k_{rxn+Q,3C*}$ is estimated from the fitting between $[^3C*]_{PTA}$ and DOC using samples from this work and Ma et al. (2023a) using an equation of $[^3C*]_{PTA} = \frac{a[DOC]}{1+b[DOC]}$ (Kaur et al., 2019). The corresponding value for $k_{rxn+Q,3C*}$ is 7.4 ($\pm$ 2.5) $\times 10^7$ L (mol C)$^{-1}$ s^{-1}, while $k_{3C*+O2} = 2.8$ ($\pm$ 0.4) $\times 10^9$ L (mol-C)$^{-1}$ s^{-1} from Kaur et al. (Kaur et al., 2019).

[h] Production rate of triplet determined by PTA, calculated as $P_{3C*,PTA} = [^3C*]_{PTA} \times k'_{3C*,PTA}$.

[i] Apparent quantum yield of $^3C*$ determined by PTA during simulated sunlight illumination, calculated as $\Phi_{3C*,PTA} = P_{3C*,PTA}/R_{abs}$.

[j] Ratio of triplet concentration determined by PTA to that determined by SYR.

[k] These two samples are the interpolations of the winter and summer samples, respectively, from our previous work (Ma et al., 2023a). $^3C^*$ concentrations were estimated by interpolating the hyperbolic regression between $[^3C^*]_{PTA}$ and concentration factor, to an equivalent extraction volume of 1 mL water/square.

[l] This field blank sample was contaminated by a pH electrode and possibly other unknown sources, leading to fast decay of PTA.

[m] Average value of each sample type. The $^3C^*$ concentration normalized by sampling duration was used in the calculation of average $[^3C*]_{PTA}$.

Section S2. Satellite images and back trajectories for wildfire samples

The figures below show satellite images of Northern California with fire points detected by the NASA Visible Infrared Imaging Radiometer Suite (VIIRS) for seven wildfire particle samples on the day of collection. The bottom panel of each figure is a 24-h back trajectory that ends at the Davis sampling site at the middle of the sample period. Back trajectories were estimated by the Hybrid Single Particle Lagrangian Integrated Trajectory (HYSPLIT) model at heights of 20, 600, and 1200 m above the ground (Rolph et al., 2017; Stein et al., 2015).
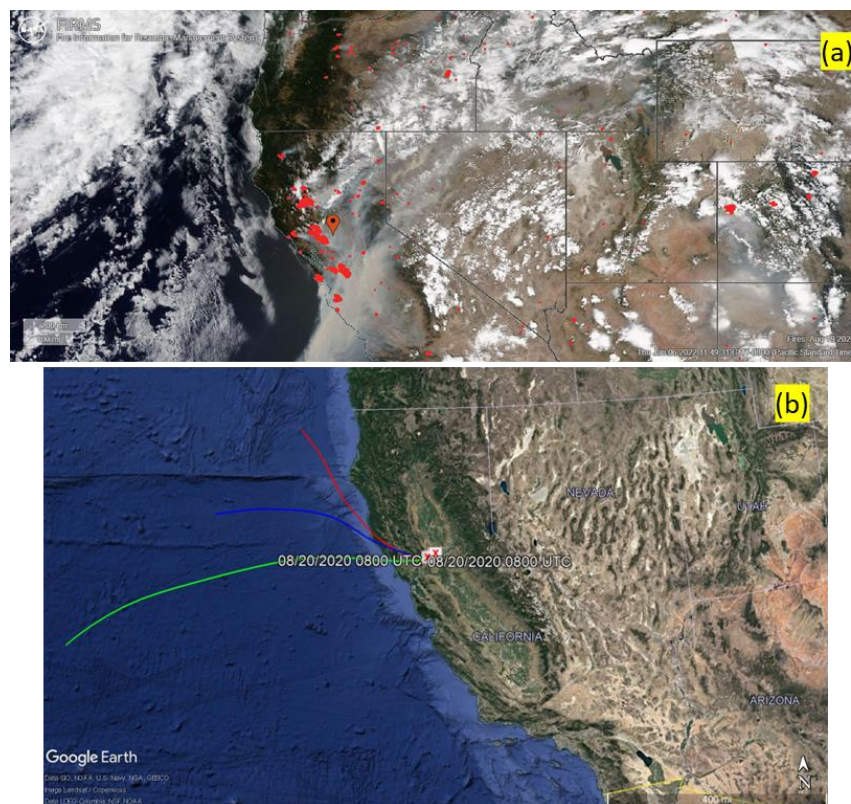
Figure S2. (a) Satellite image on 19 August 2020, with fires detected by VIIRS labeled by red dots. The location symbol represents Davis CA. (b) 24-hr back trajectories from the sampling site at a height of 20 m (red), 600 m (blue), and 1200 m (green) above the ground. It took approximately 1-2 h for the smoke plume from the Lake Berryessa area west of Davis to be transported to the sampling site.
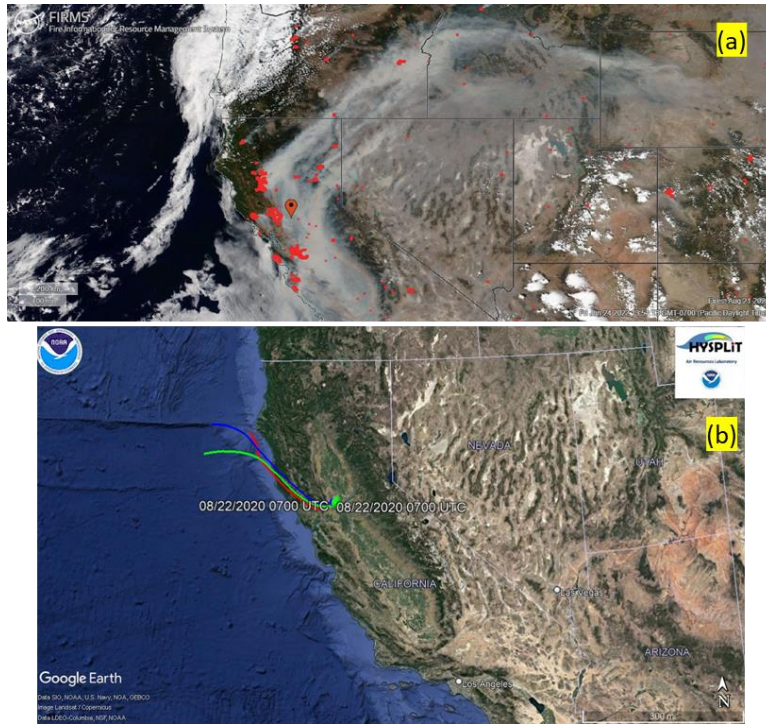
Figure S3. (a) Satellite image on 22 August 2020, with fires detected by VIIRS labeled by red dots. The location symbol represents Davis CA. (b) 24 hr back trajectories ending at the sampling site at heights of 20 m (red), 600 m (blue), and 1200 m (green) above the ground. It took approximately 1-2 h for the smoke plume from the Lake Berryessa area west of Davis to be transported to the sampling site.
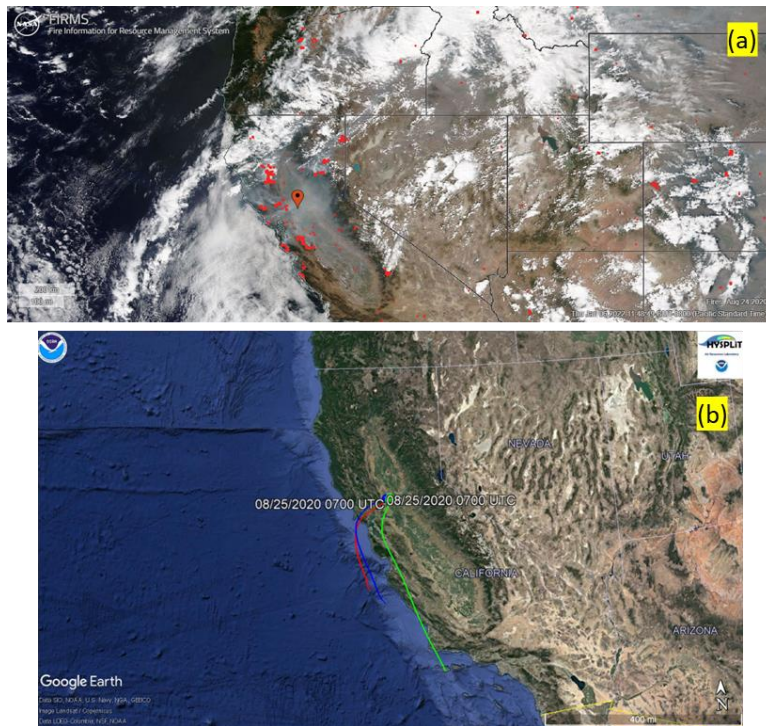
Figure S4. (a) Satellite image on 24 August 2020, with fires detected by VIIRS labeled by red dots. The location symbol represents Davis CA. (b) 24 hr-back trajectories ending at the sampling site at heights of 20 m (red), 600 m (blue), and 1200 m (green) above the ground.
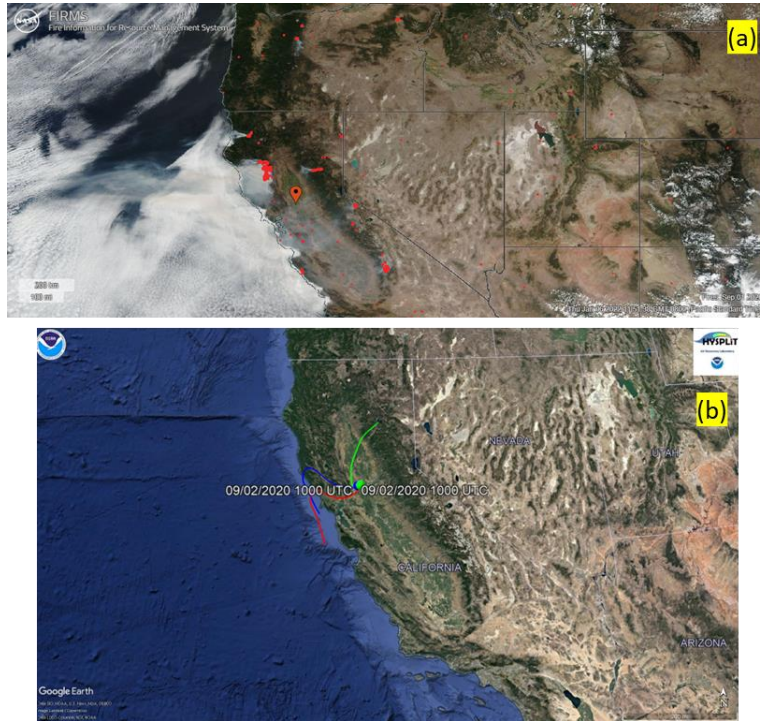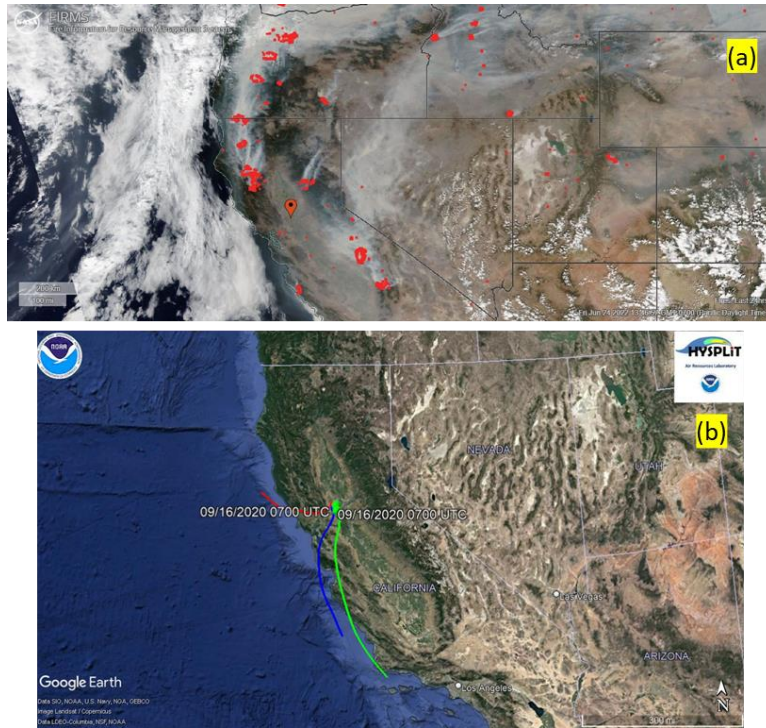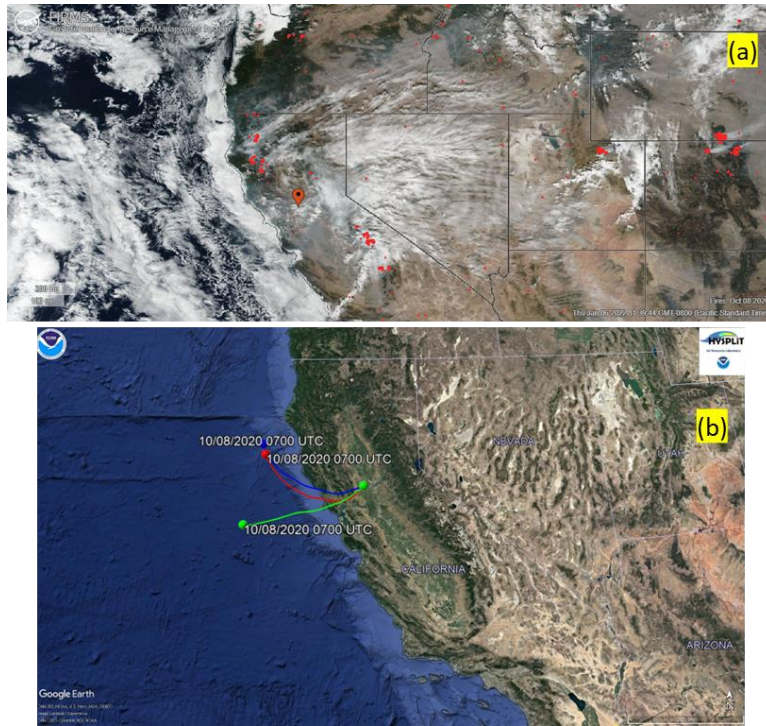
Figure S5. (a) Satellite image on 1 September 2020, with fires detected by VIIRS labeled by red dots. The location symbol represents Davis CA. (b) 24-hr back trajectories ending at the sampling site at heights of 20 m (red), 600 m (blue), and 1200 m (green) above the ground. Wildfire plumes from the Mendocino National Forest and Chico area took approximately 9 -12 h to transport to Davis.
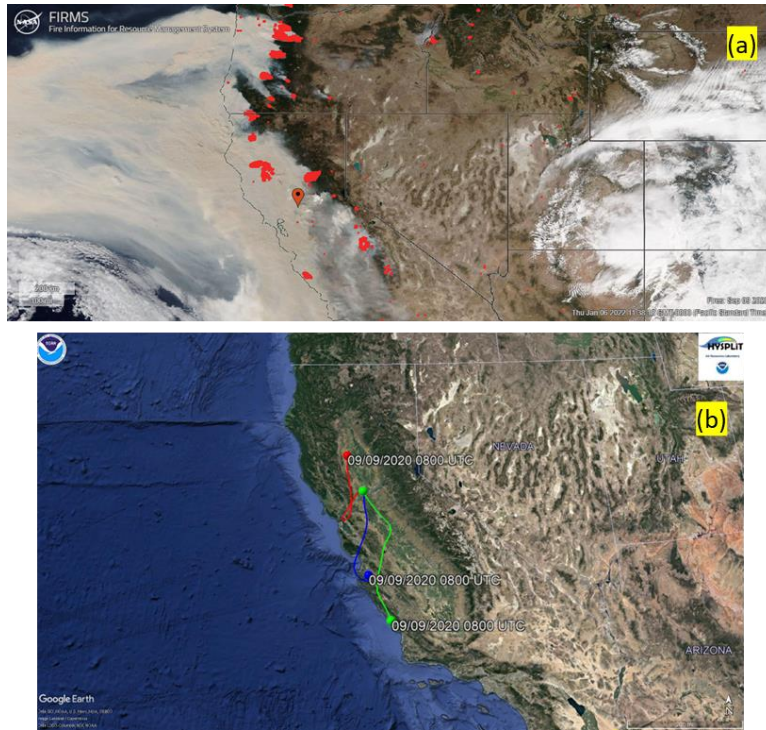
Figure S6. (a) Satellite image on 9 September 2020, with fires detected by VIIRS labeled by red dots. The location symbol represents Davis CA. (b) 24-hr back trajectories ending at the sampling site at heights of 20 m (red), 600 m (blue), and 1200 m (green) above the ground. Wildfire plumes from the Mendocino National Forest, the Chico area, and Oregon required approximately 7 to 24 h to transport to Davis during this time.

Figure S7. (a) Satellite image on 15 September 2020, with fires detected by VIIRS labeled by red dots. The location symbol represents Davis CA. (b) 24-hr back trajectories ending at the sampling site at heights of 20 m (red), 600 m (blue), and 1200 m (green) above the ground. Because the back trajectories do not pass through the burning regions it is difficult to estimate a plume aging time.

Figure S8. (a) Satellite image on 10 October 2020, with fire points detected by VIIRS labeled by red dots. The location symbol represents Davis CA. (b) 24-hr back trajectories ending at the sampling site at heights of 20 m (red), 600 m (blue), and 1200 m (green) above the ground. The back trajectories appeared not to pass through the burning areas directly, making it difficult to estimate the aging time.
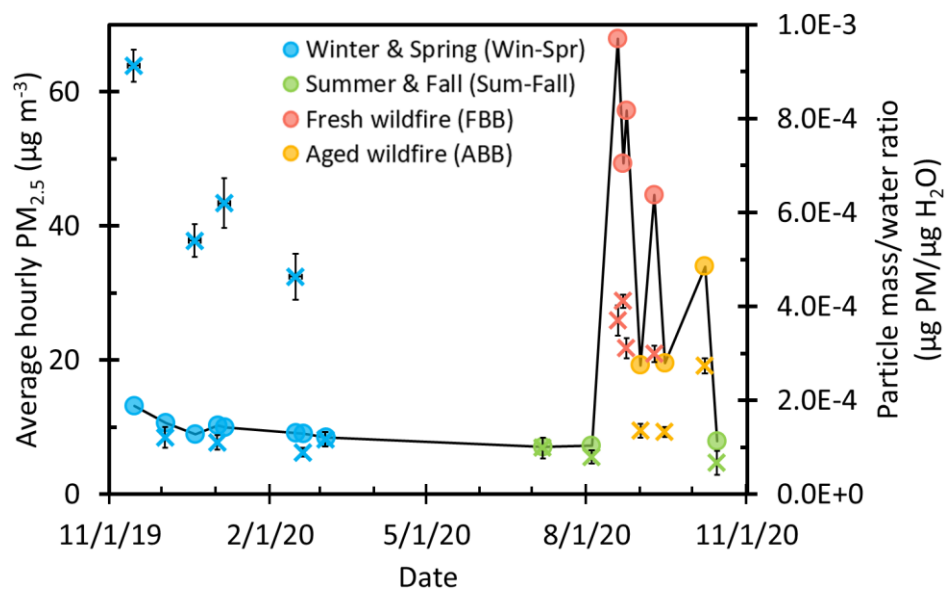
Figure S9. Average PM$_{2.5}$ concentration during sampling period (circles) from a regulatory monitor during each sampling period and measured particle mass/water mass ratios (crosses) from filter extracts for each sample. Vertical error bars represent ±1 standard deviation, while horizontal error bars represent the duration of sampling (either 1 or 7 days).
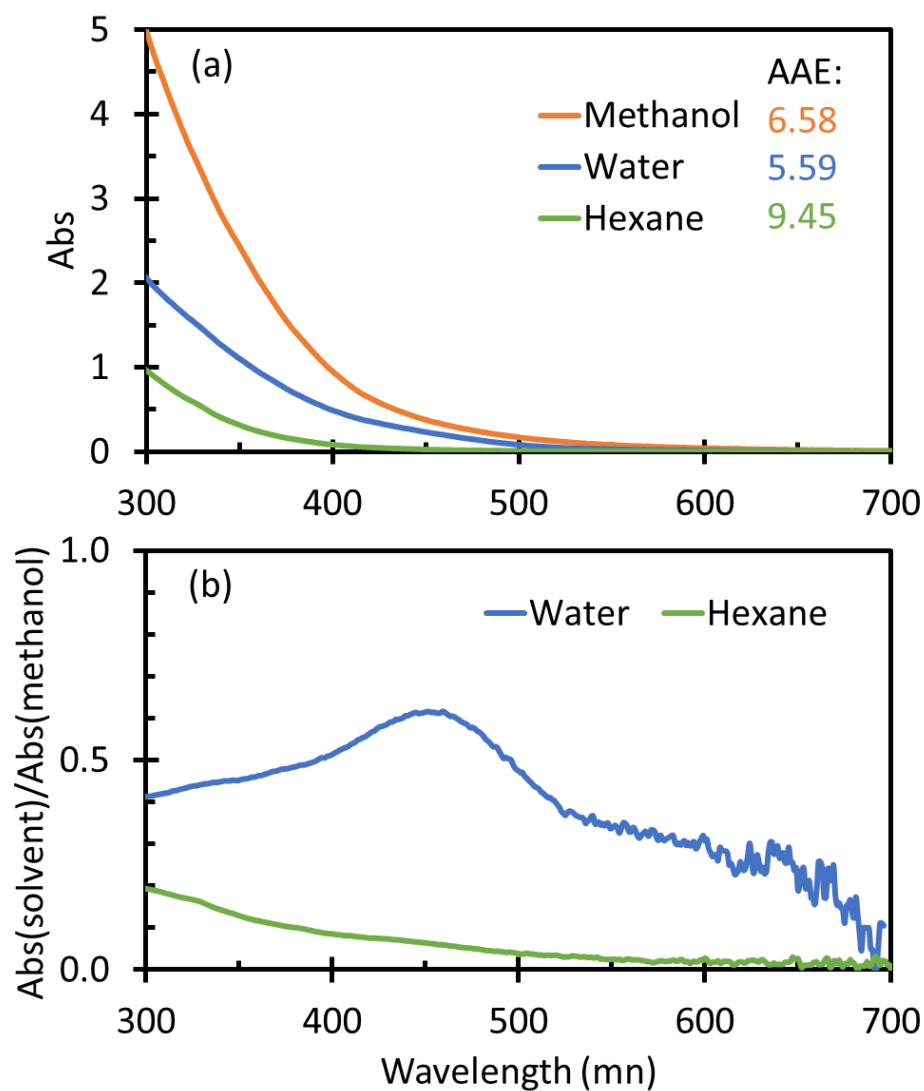
Figure S10. (a) UV-Vis spectra of different solvent extracts of the particle sample collected on 8/19/2020. Each line represents the absorbance spectrum for a square of filter that was extracted in the listed solvent then filtered. AAE values were determined for each spectrum based on absorbance over 300 to 450 nm. Spectra were measured in 1-cm cuvettes. (b) Ratio of the absorbance in the water (blue) and hexane (green) extracts to the absorbance of the methanol extract.
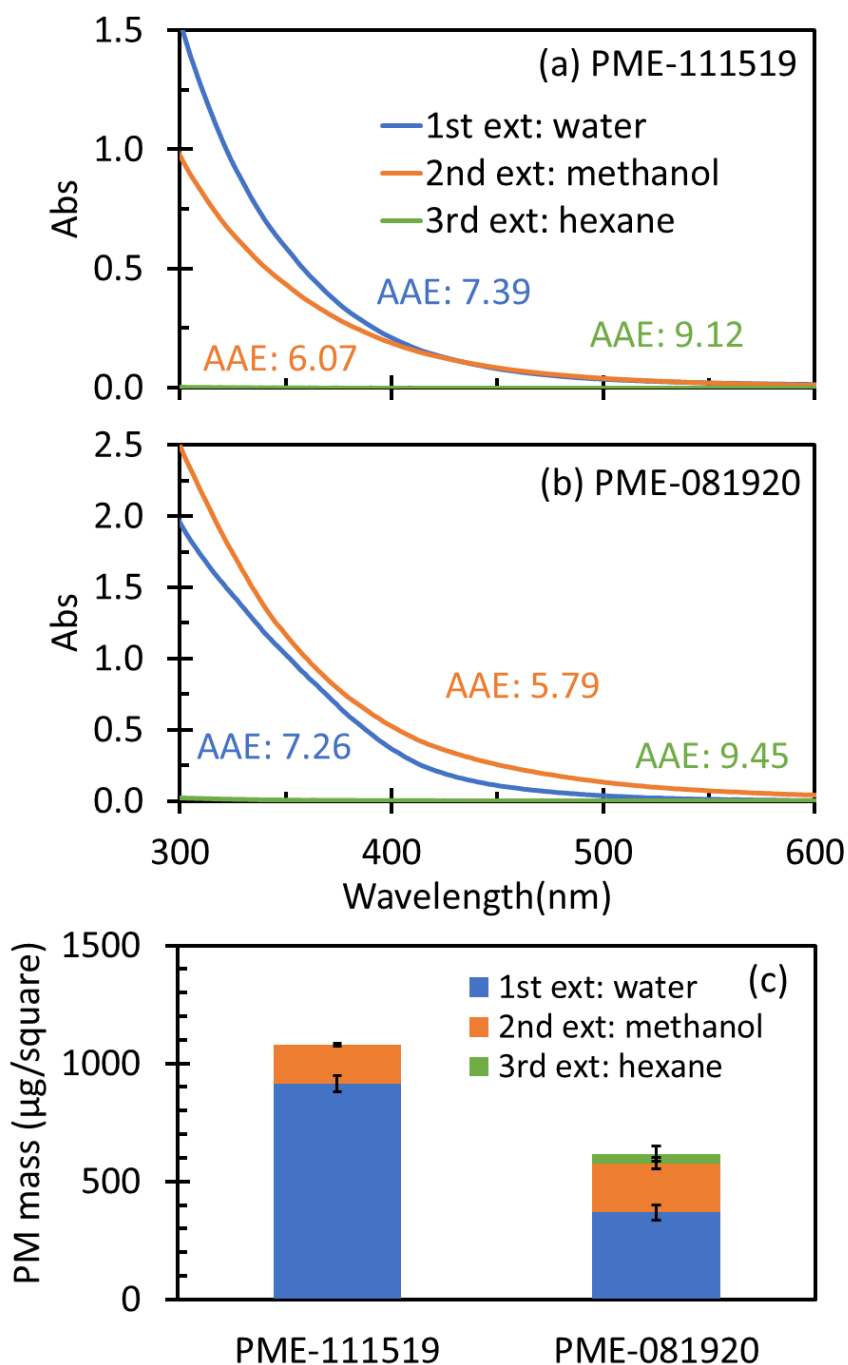
Figure S11. UV-Vis spectra for sequential extracts of a given filter square, each with 1.0 mL of the solvent listed, as measured in a 1-cm cuvette. The blue line or bar represents the first extraction, which was with water; the orange line or bar represents the second extraction, which was in methanol, and the green line or bar represents the third extraction, which was done with hexane. Panel (a) shows results for sample PME-111519, while panel (b) is for PME-081920. Panel (c) shows the particle mass extracted per filter square in the sequential extraction sequence with water, methanol, and hexane. The particle mass extracted by hexane in PME-111519 was not measured.
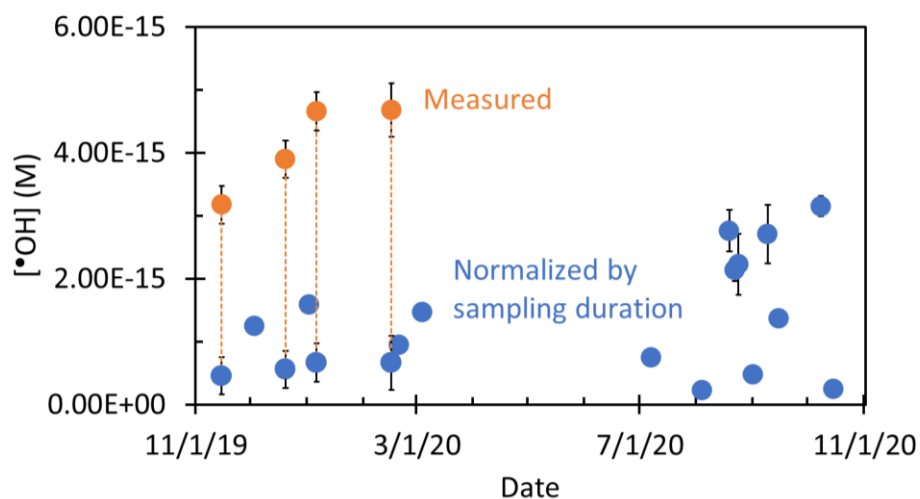
Figure S12. Comparison between measured •OH concentrations (orange) and values normalized by sampling duration in four 7-day samples (blue). Figure 4 shows the •OH data normalized by PM mass/water mass ratio, which was what we used as the standard normalization for these 7-day samples.
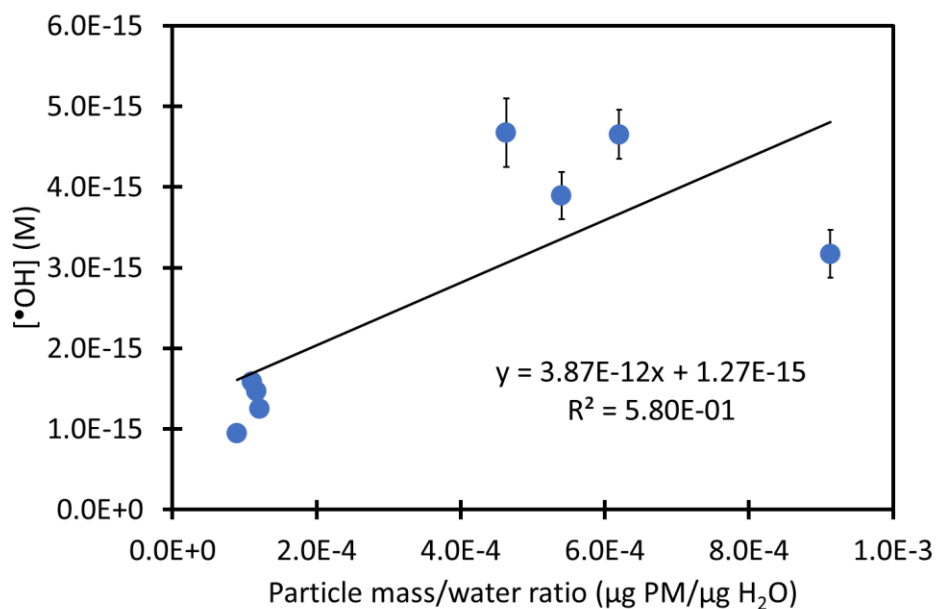

Figure S13. Dependence of hydroxyl radical concentration on particle mass/water mass ratio for Winter & Spring samples. The line represents the linear regression.
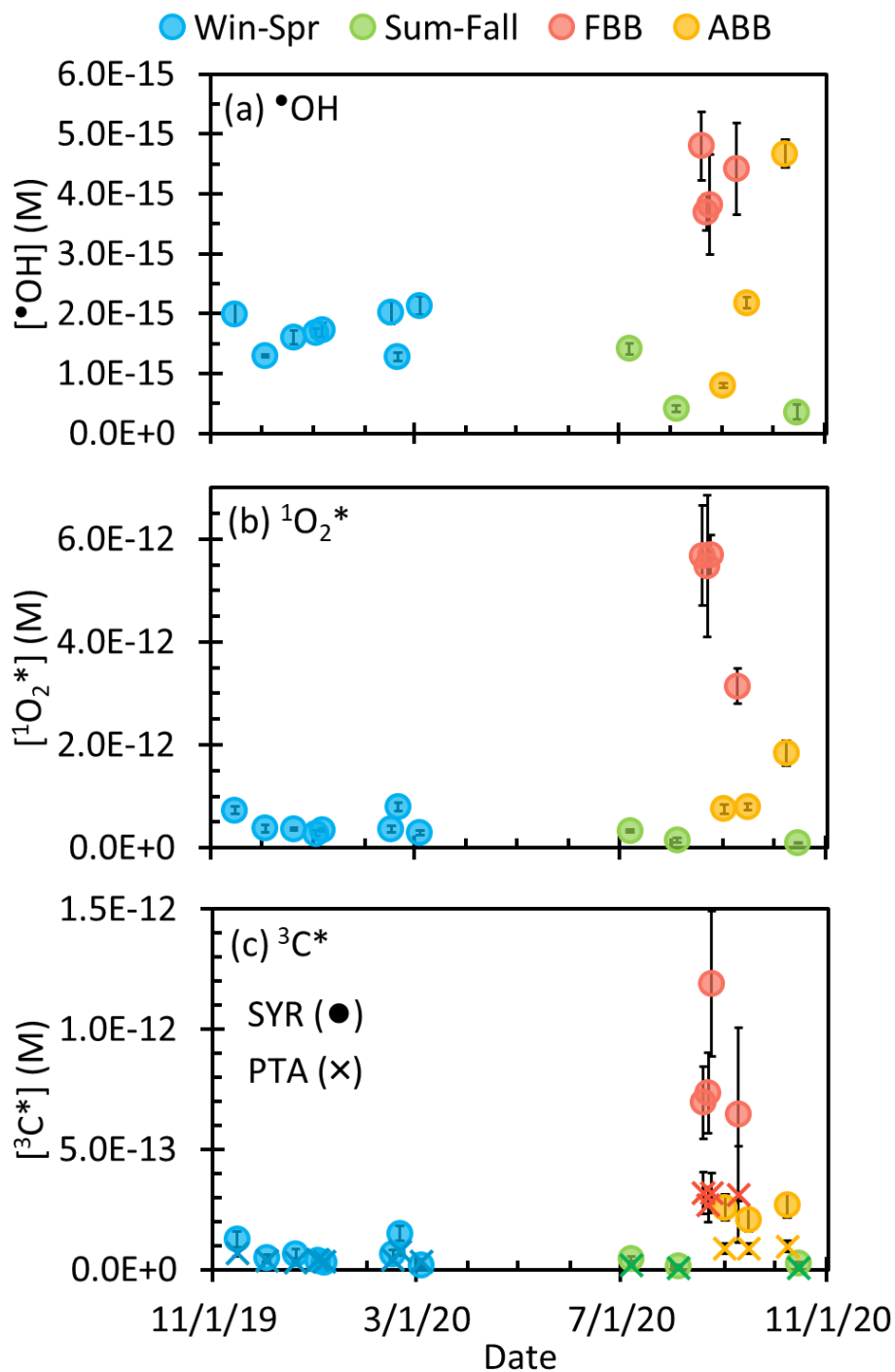
Figure S14. Steady-state concentrations of (a) hydroxyl radical, (b) singlet molecular oxygen, and (c) oxidizing triplet excited states of light-absorbing organics determined by syringol (SYR) and (phenylthio)acetic acid (PTA, cross symbols) in particle extracts. Concentrations are normalized to the midday sunlight of each sampling period to account for the seasonal differences in actinic flux and the seven-day samples were normalized to the expected one-day result as described in section 3.3.1 and Table S9.
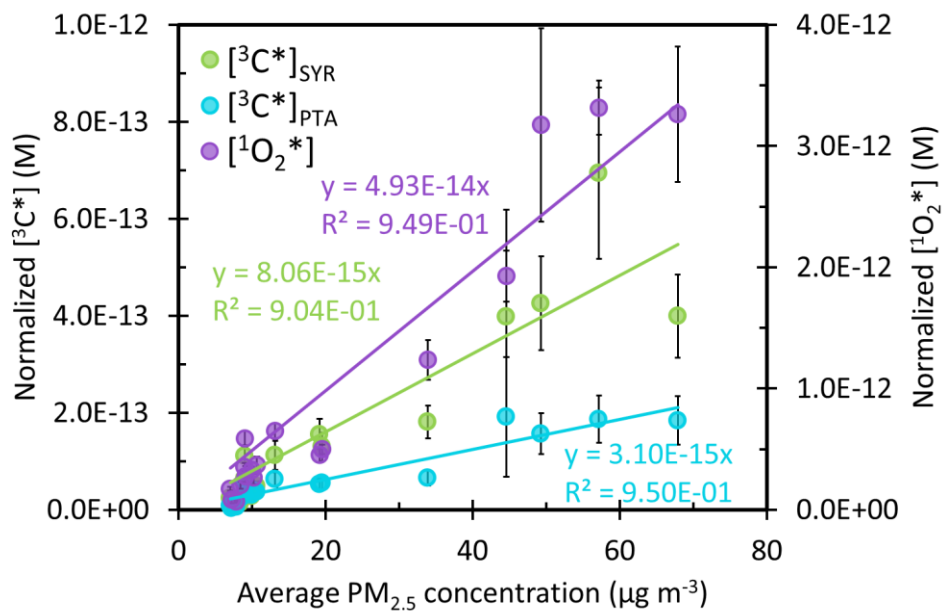
Figure S15. Normalized singlet oxygen (purple, right *y*-axis) and triplet excited state of organic matter determined by syringol (green) and (phenylthio)acetic acid (blue) as a function of average $PM_{2.5}$ concentration. Solid lines are linear regressions with the *y*-intercepts fixed at zero.
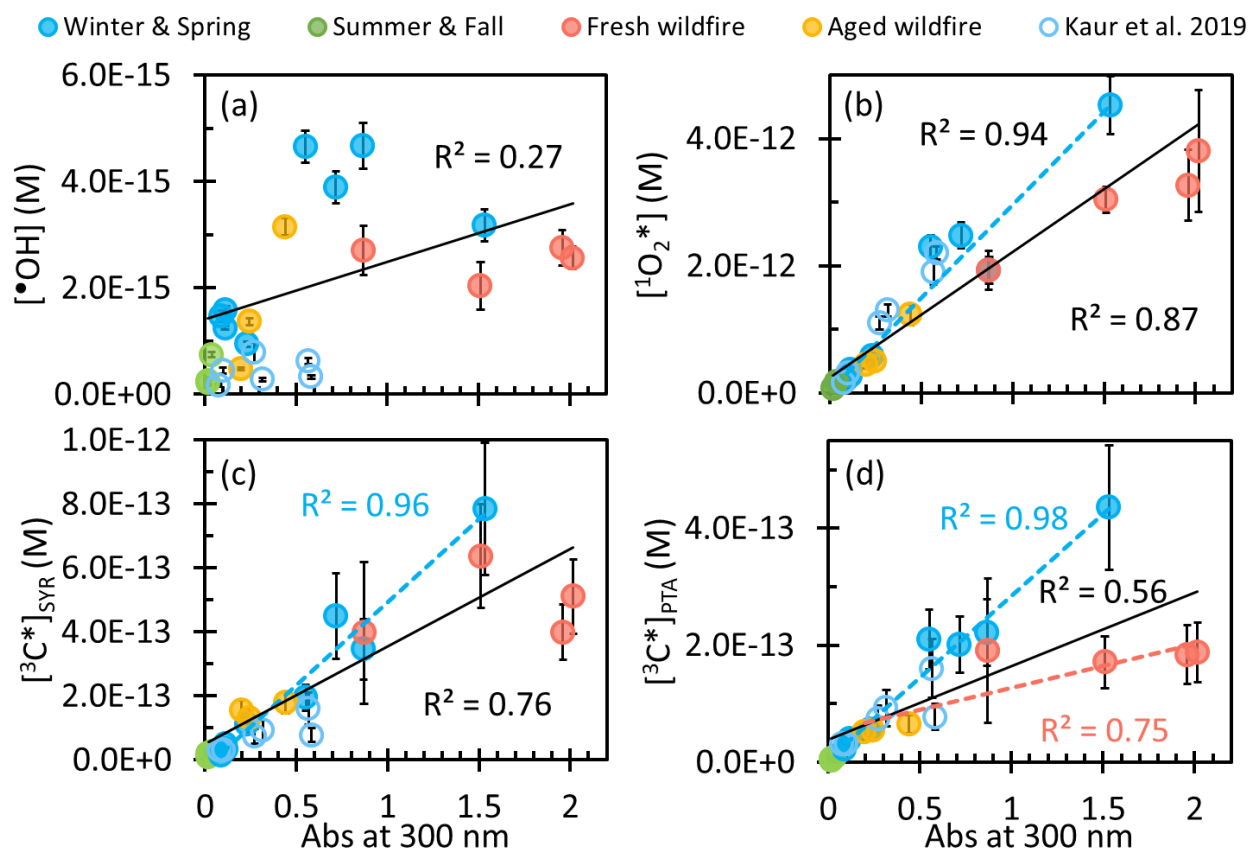
Figure S16. Steady-state concentrations of (a) hydroxyl radical, (b) singlet molecular, and oxidizing triplet excited states of organic matter determined by (c) syringol and (d) (phenylthio)acetic acid as a function of absorbance at 300 nm for each sample type (solid circles). Previous measurements made on Davis winter particle extracts are shown by open blue circles (Kaur et al., 2019). Solid lines are linear regressions between oxidant concentrations of all samples in this work and extract absorbance in a 1-cm cell. Blue dashed lines are the linear regressions of our Win-Spr samples, while the red dashed line is a regression of the FBB and ABB samples.
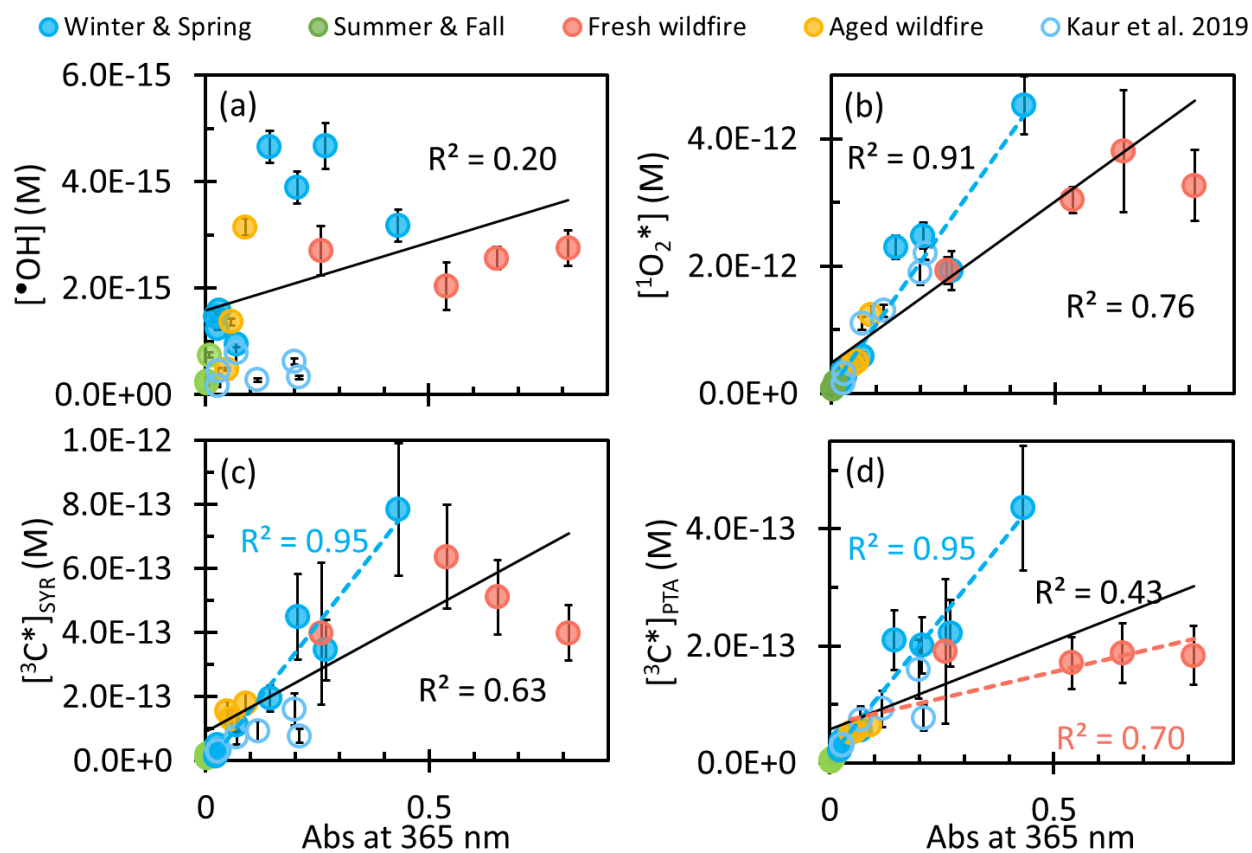
Figure S17. Steady-state concentrations of (a) hydroxyl radical, (b) singlet molecular, and oxidizing triplet excited state of organic matter determined by (c) syringol and (d) (phenylthio)acetic acid as a function of absorbance (in a 1 cm cell) at 365 nm for each sample type (solid circles). Previous measurements made in Davis winter particle extracts are included (open circles) (Kaur et al., 2019). Solid lines are linear regressions between oxidant concentration and absorbance for all samples in our current work. Blue dashed lines are the linear regressions of current Win-Spr samples, while the red dashed line is the regression of the combined FBB and ABB samples.
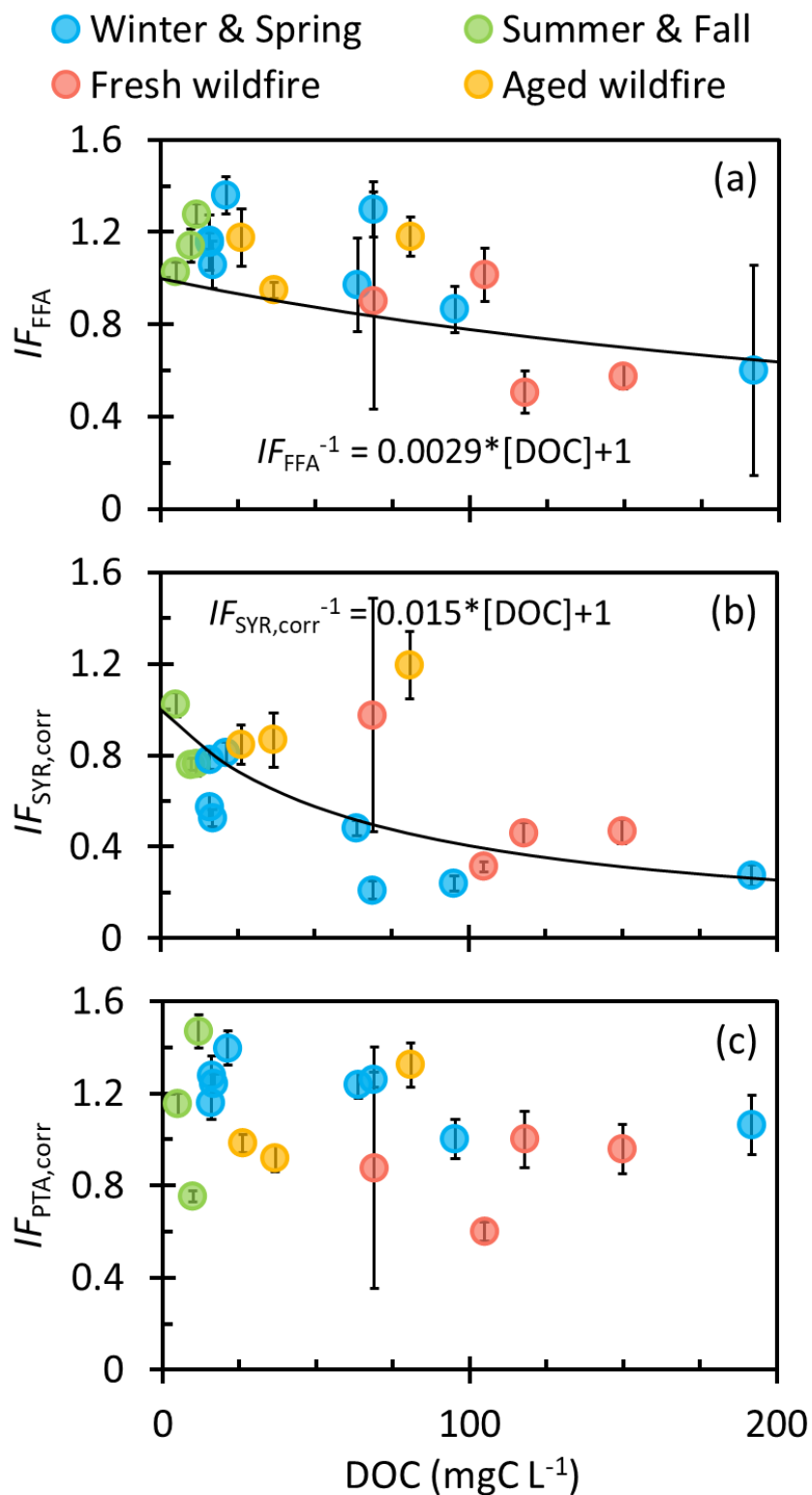
Figure S18. Inhibition factor of (a) furfuryl alcohol, and corrected inhibition factors of (b) syringol and (c) (phenylthio)acetic acid as a function of dissolved organic carbon. Solid lines represent linear regressions of $IF_P^{-1} = a[DOC] + b$ (Ma et al., 2023b; Wenk et al., 2011).
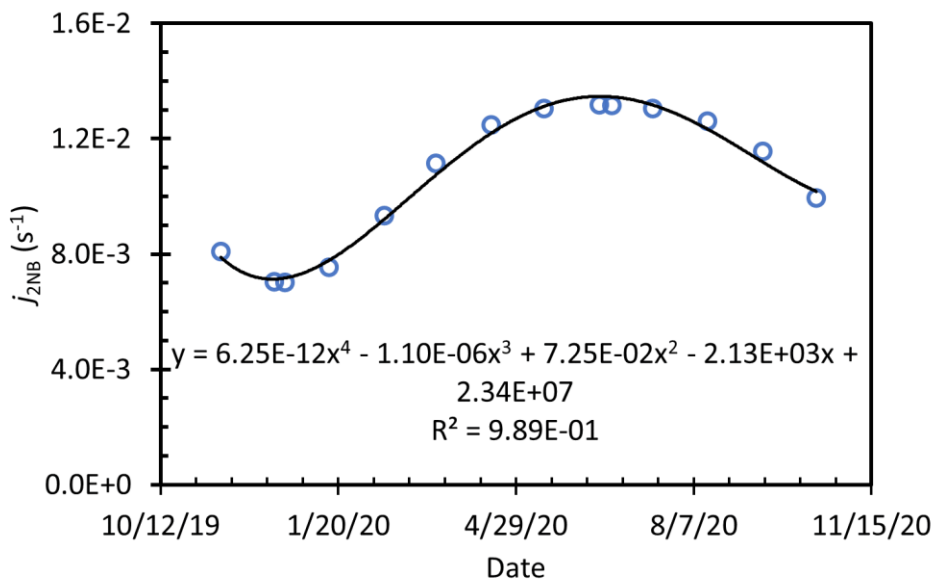
Figure S19. Estimated midday j_{2NB} values as a function of date based on TUV actinic fluxes (points) and the corresponding 4th-order polynomial fit (solid line). Details about the estimation of j_{2NB} values are provided in Section S3.

Section S3. Seasonal variation of j_{2NB}

We obtained the modeled actinic flux (photons s^{-1} nm^{-1} cm^{-2}) on the midday of the 15th of each month in Davis CA (38.545 ° N, 121.741 ° W) from November 2019 to October 2020 from the Tropospheric Ultraviolet and Visible (TUV) Radiation Model version 5.3 (https://www.acom.ucar.edu/Models/TUV/Interactive_TUV/, last access: 7 August 2022). For the TUV model runs, other input parameters like ozone column and aerosols were set at default values:

Ozone column: 300 du

Surface albedo: 0.1

Ground elevation & Measurement altitude: 0 km asl

Aerosols: Option depth: 0.235; S-S Alb: 0.990; Alpha: 1.000.

j_{2NB} values for each date were calculated using (Galbavy et al., 2010):

$$j_{2NB} = 2.303 \times (10^3 \ cm^3 L^{-1} \div N_A) \times \sum_{\lambda} (I'_{\lambda} \times \Delta\lambda \times \varepsilon_{2NB,\lambda} \times \Phi_{2NB,\lambda})$$

where N_A is Avogadro's number, I'_{λ} is the actinic flux (photons s^{-1} nm^{-1} cm^{-2}), $\Delta\lambda$ is the wavelength interval between actinic flux data points (1 nm here), ε_{2NB} is the base-10 molar absorption coefficient of 2-nitrobenzaldehyde (M^{-1} cm^{-1}) (Galbavy et al., 2010), and Φ_{2NB} is the 2NB quantum yield (0.41 molecule photon^{-1}, independent of wavelength (Galbavy et al., 2010)). From our calculations, j_{2NB} on the midday of the winter solstice is 0.0053 s^{-1}, which is lower than the value (0.0070 s^{-1}) measured in Davis on this day

(Anastasio and McGregor, 2001). To approximately compensate for the difference between the measured and modeled values, we added 0.0017 s^{-1} to each calculated j_{2NB} value and plotted them as a function of date (Figure S19). We then fitted the data with a 4th-order polynomial with Excel dates as x values, and use this regression to calculate j_{2NB} on each day of sampling. The calculated j_{2NB} values are in Table S9.

Table S9. Calculated j_{2NB} values for each sample

Sample Type	Sample ID	j_{2NB} (s^{-1})[a]
Winter & Spring	PME-111519	0.0079
	PME-120319	0.0072
	PME-122019	0.0072
	PME-010220	0.0074
	PME-010620	0.0075
	PME-021620	0.0093
	PME-022020	0.0095
	PME-030420	0.010
Summer & Fall	PME-070720	0.013
	PME-080420	0.013
	PME-101520	0.010
Fresh wildfire	PME-081920	0.012
	PME-082220	0.012
	PME-082420	0.012
	PME-090920	0.011
Aged wildfire	PME-090120	0.012
	PME-091520	0.011
	PME-100820	0.010
Averages		
Winter & Spring		0.0083
Summer & Fall		0.012
Fresh wildfire		0.012
Aged wildfire		0.011

[a] Values are calculated for midday on the middle day of each sampling period in Davis; see Section S3.
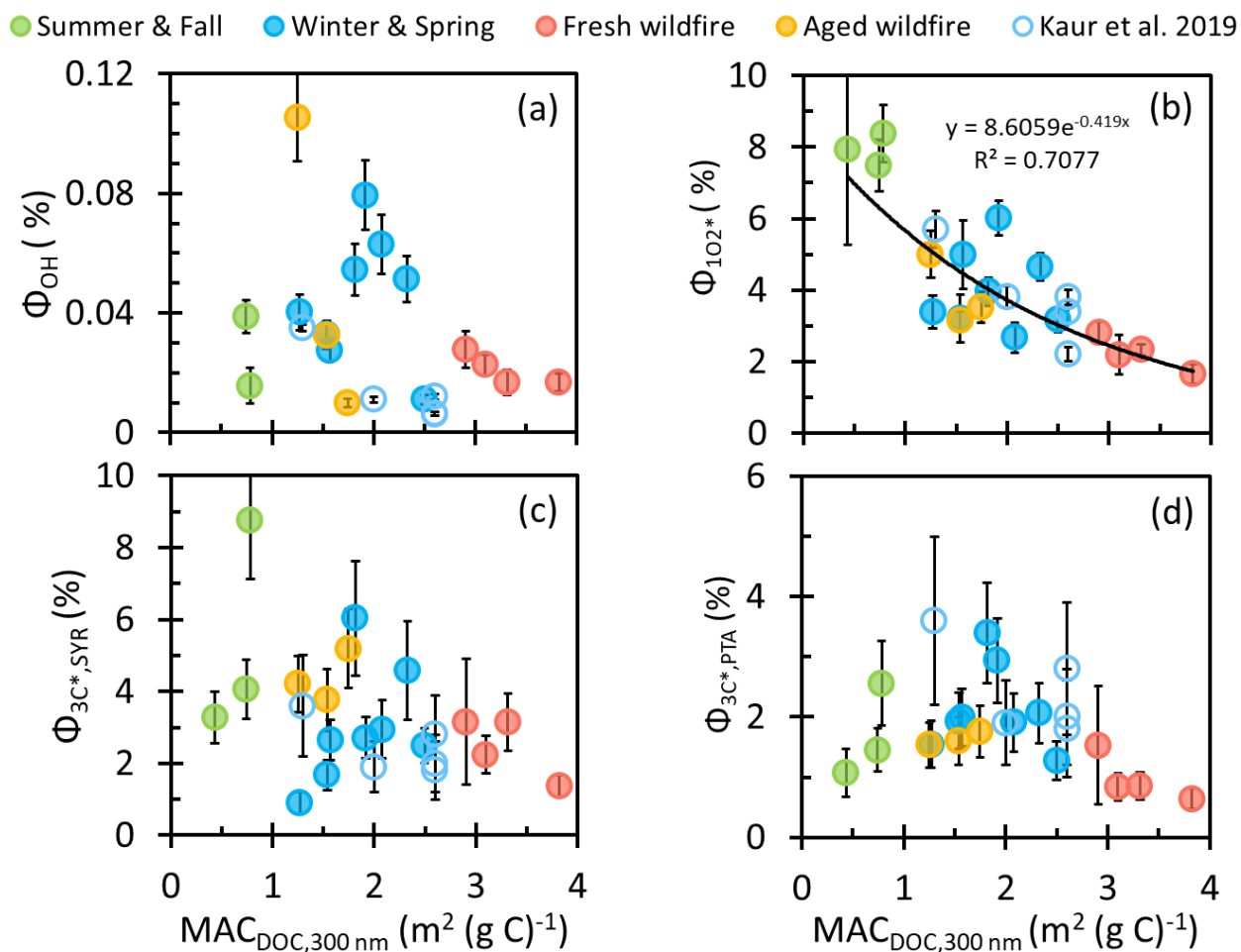
Figure S20. Apparent quantum yields of (a) hydroxyl radical, (b) singlet molecular oxygen, and oxidizing triplet excited states of organic matter determined by (c) syringol and (d) (phenylthio)acetic acid as a function of DOC-normalized mass absorption coefficient at 300 nm (solid circles). Previous measurements made in Davis winter particle extracts are shown in blue open circles (Kaur et al., 2019). The solid black line represents an exponential regression to all of the $^1O_2^*$ data in this work, not including data from Kaur et al. (2019).
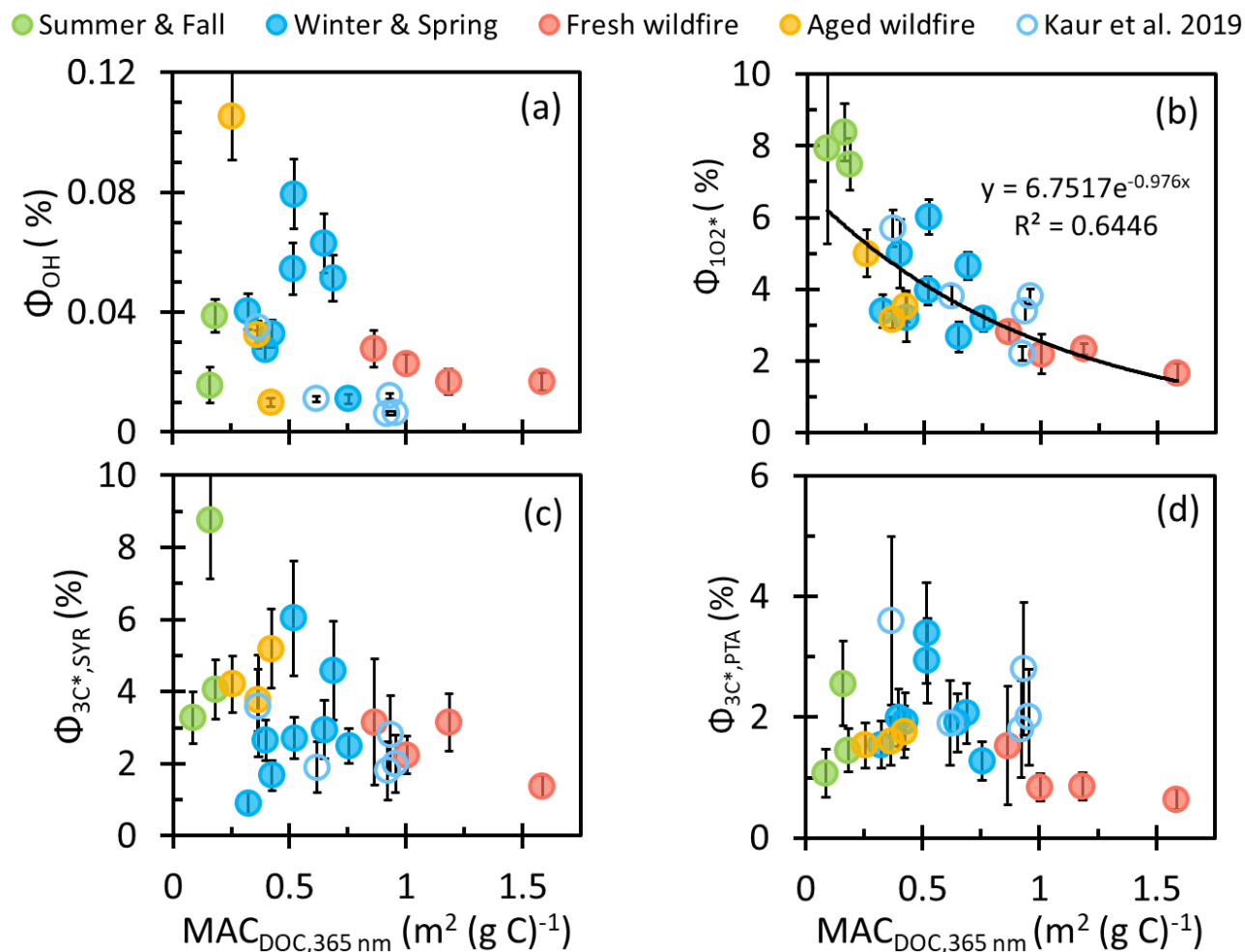
Figure S21. Apparent quantum yields of (a) hydroxyl radical, (b) singlet molecular oxygen, and oxidizing triplet excited states of organic matter determined by (c) syringol and (d) (phenylthio)acetic acid as a function of DOC-normalized mass absorption coefficient at 365 nm (solid circles). Previous measurements made in Davis winter particle extracts are shown in blue open circles (Kaur et al., 2019). The solid black line represents an exponential regression to all of the $^1O_2*$ data in this work, not including data from Kaur et al. (2019).
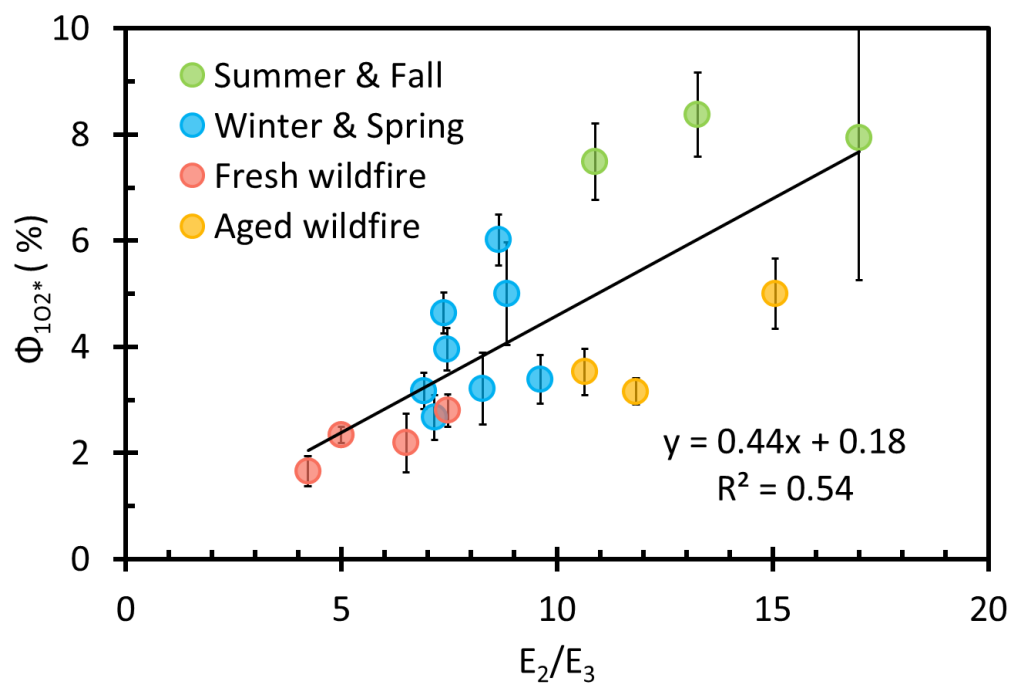
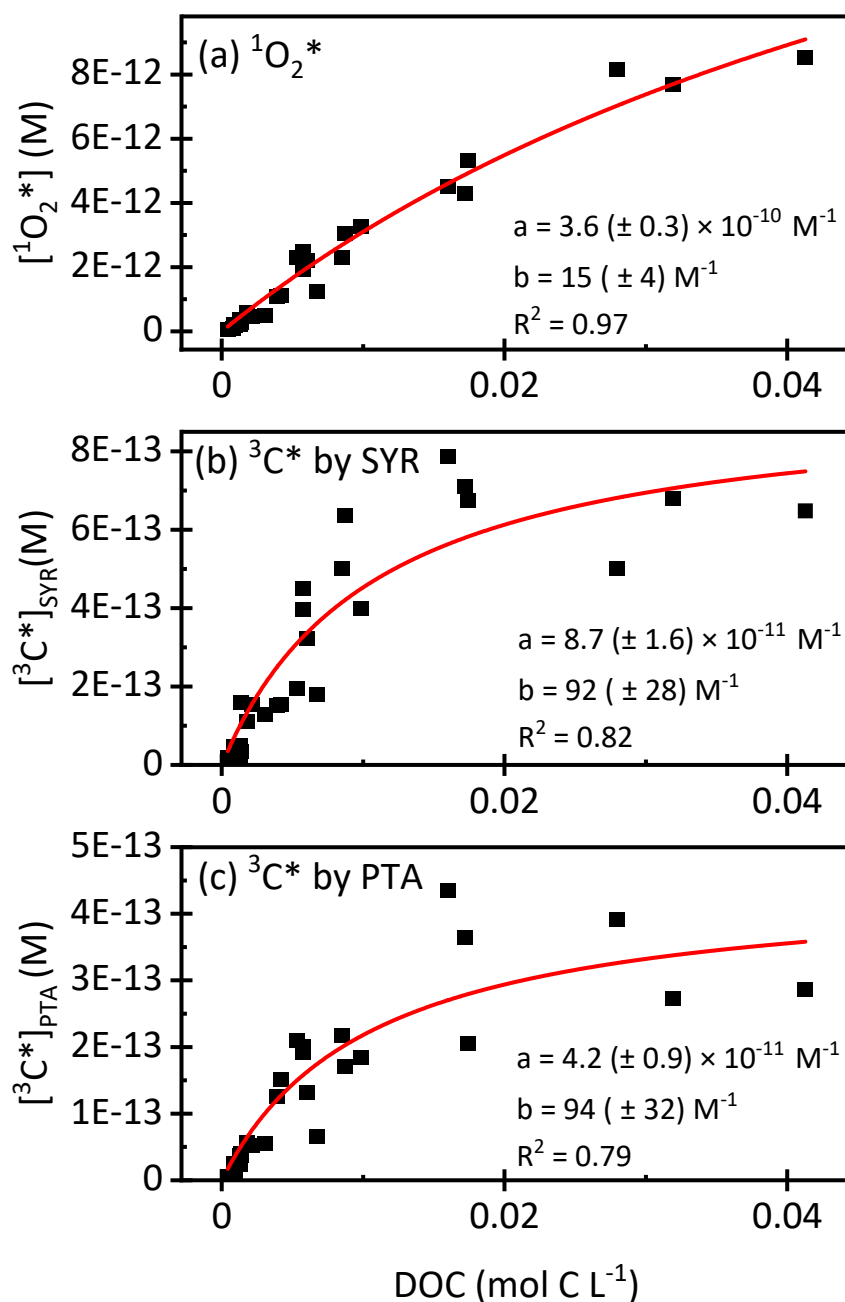**Figure S22.** Apparent quantum yields of $^1O_2^*$ as a function of E_2/E_3.

Figure S23. Dependence of (a) $^1O_2*$, (b) $^3C*$ determined by SYR, and (c) $^3C*$ determined by PTA on dissolved organic carbon. Solid lines represent hyperbolic regressions with the equation $[Ox] = \frac{a[DOC]}{1+b[DOC]}$. The equation is derived in Kaur et al. (2019); as described in this past work, we obtain the rate constant for quenching and reaction of the oxidant by DOC using the fitted value of the b parameter. The data points include the two previous measurements made in Davis winter particle and wildfire particle extracts from Ma et al. (2023a), but not data from Kaur et al. (2019).
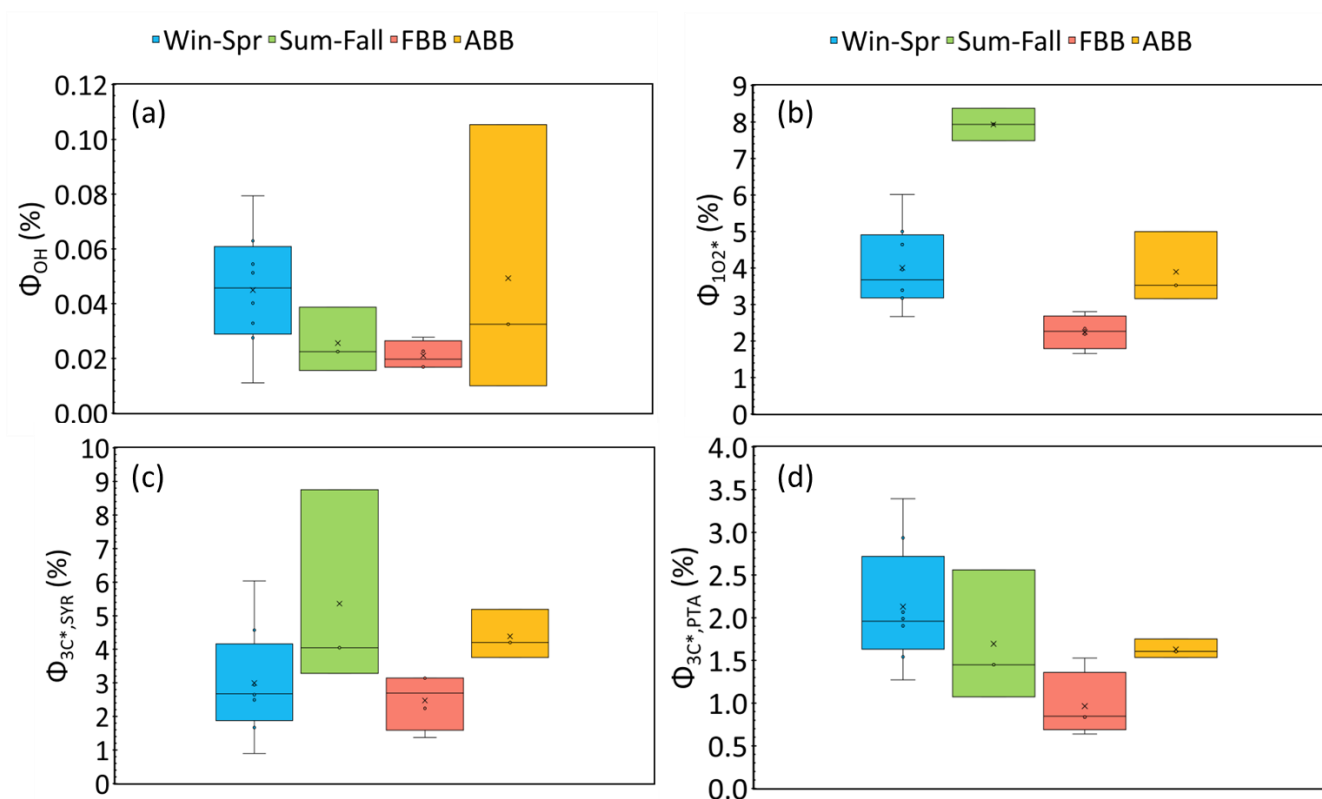
Figure S24. Box plots of apparent quantum yields of (a) $^\bullet$OH, (b) $^1O_2$*, (c) ^{3}C* determined by SYR, and (d) ^{3}C* determined by PTA for each sample type. For each box, the horizontal line within the box is the median value, while the top and bottom of the box represent the 75th and 25th percentiles, and the cross symbol and open circles are the mean value and data points, respectively. Whiskers represent the minimum and maximum data points.
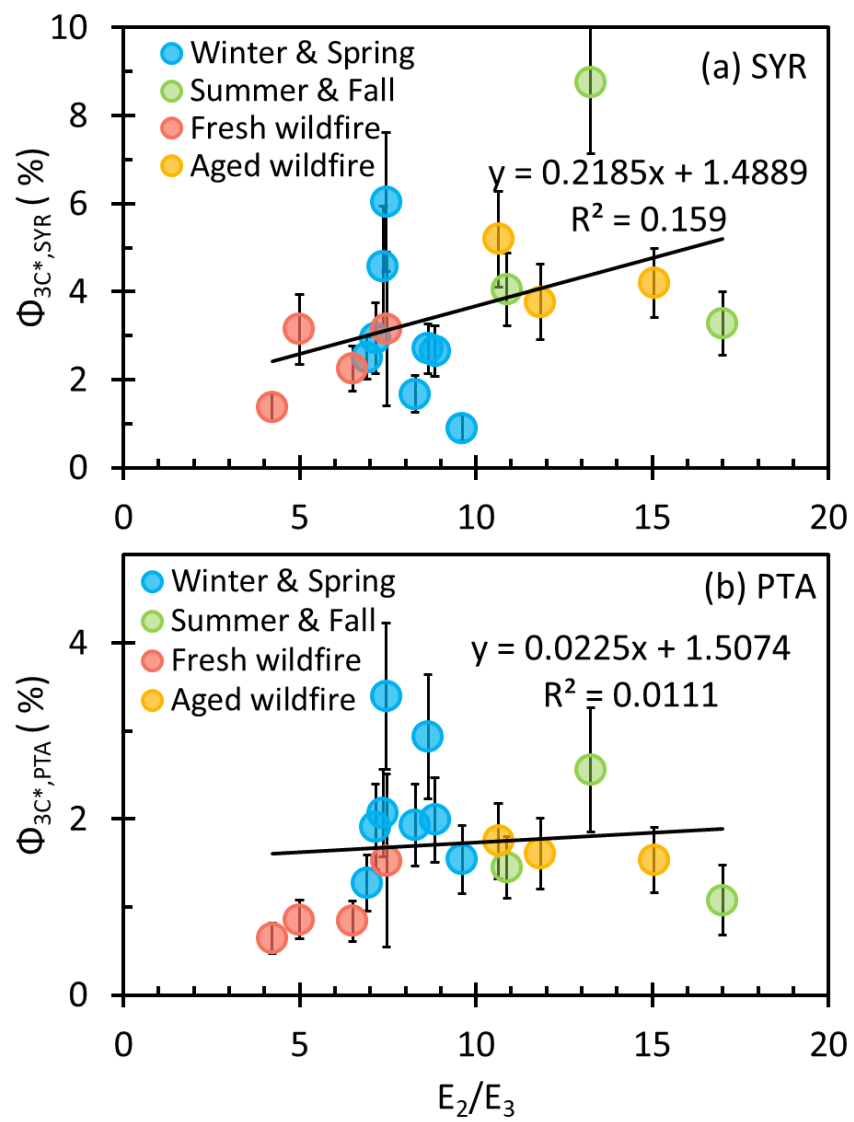
Figure S25. Apparent quantum yields of $^3C^*$ determined by (a) SYR and (b) PTA as a function of E_2/E_3.
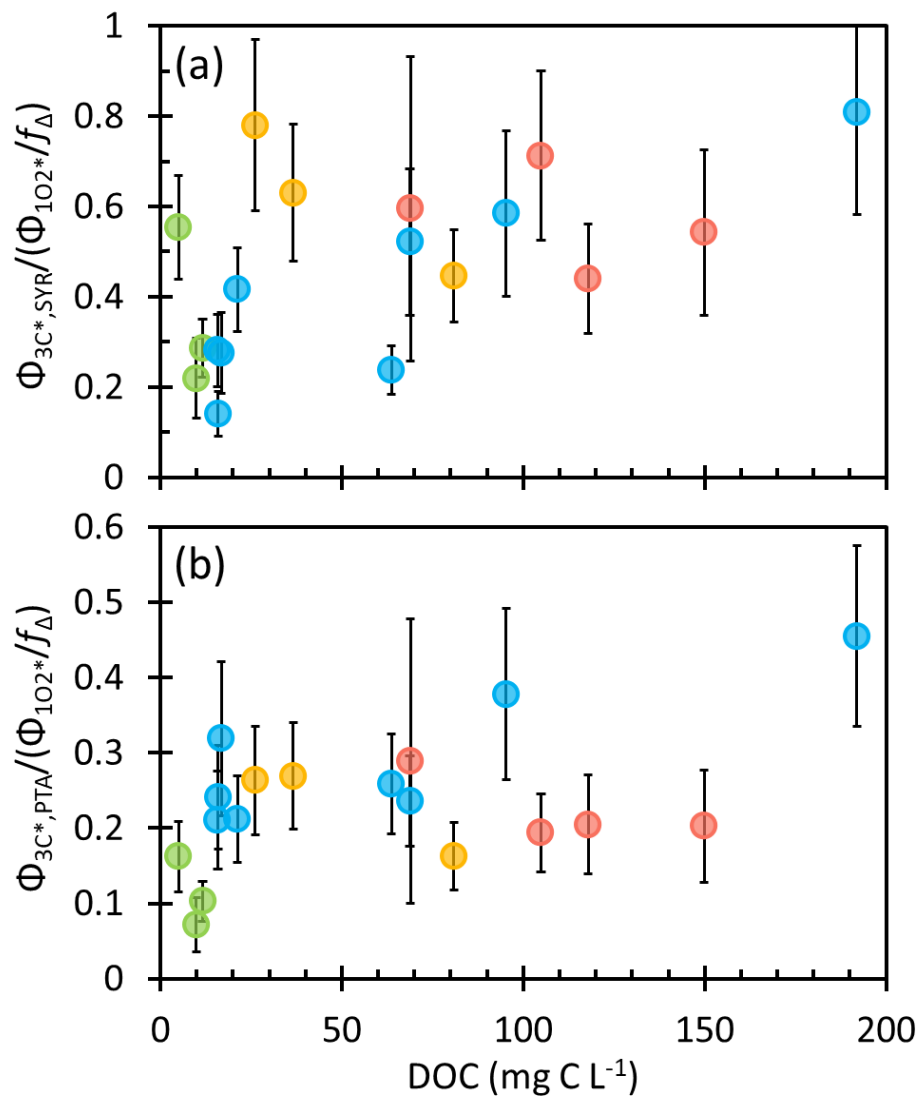
Figure S26. Approximate fraction of the total triplet pool (i.e., those that can generate singlet oxygen) that can oxidize (a) SYR and (b) PTA as a function of DOC. Based on the averages (± 1 σ) for these two plots (0.47 (± 0.20) and 0.24 (± 0.09) for (a) and (b), respectively), approximately 24 % of the total triplets are strongly oxidizing (determined as the PTA average fraction) and roughly 23 % of the total triplets are weakly oxidizing (determined as the SYR average fraction minus the PTA average).

Section S4. Extrapolating photooxidant concentrations in PME to aerosol liquid water (ALW) conditions

Photooxidant concentrations that we measured in PM extracts represent dilute conditions similar to cloud/fog waters, while our goal is to estimate photooxidant concentrations in aerosol liquid water, which is orders of magnitude more concentrated. To predict photooxidant concentrations in ALW, we quantified photooxidant kinetics (i.e., oxidant formation rates and loss rate constants) for each sample type as a function of particle mass concentration and then extrapolate to ALW conditions (Kaur et al., 2019; Ma et al., 2023a).

We start by considering hydroxyl radical. Based on results from the three samples that have been studied (Kaur et al., 2019; Ma et al., 2023a), there are at least two ways that the kinetics for $^\bullet$OH production vary as a function of extract concentration. In the two winter samples studied, the $^\bullet$OH concentration is independent of DOC concentration (a proxy for extract concentration), which we interpret to mean that both the production rate (P_{OH}) and $^\bullet$OH sink (k'_{OH}) linearly increase with DOC (Kaur et al., 2019; Ma et al., 2023a). However, in the third sample, which was collected in the summer and heavily influenced by relatively fresh biomass burning emissions, the $^\bullet$OH concentration increases with DOC, which suggests that the major $^\bullet$OH production pathway is a bimolecular reaction whose rate increases as the square of extract concentration (Ma et al., 2023a).

In our current work, we do not observe significant differences in the relationships of [$^\bullet$OH] and DOC among the four sample types (Figure 5). Therefore, to predict [$^\bullet$OH] in ALW for our current samples, we use the average P_{OH} values of the winter and summer samples at a given PM mass/water mass ratio in Ma et al. (2023a) and do not consider the small differences among sample types. We similarly use the average for the winter and summer k'_{OH} values at each PM mass/water mass ratio (Ma et al., 2022a). Figure S28 shows the average [$^\bullet$OH] calculated with $^\bullet$OH production only from aqueous reactions (Fig. S28a) and considering both aqueous reactions and gas-phase mass transport (Fig. S28b). Figure S28a shows that the average $^\bullet$OH prediction fits well with the measured [$^\bullet$OH] in more concentrated PME, but overestimates [$^\bullet$OH] in PME with low particle mass/water mass ratio, i.e., in more dilute extracts. Including gas-phase mass transport of $^\bullet$OH (Fig. S28b) increases the predicted [$^\bullet$OH], most notably at low particle mass/water mass ratios where $^\bullet$OH transport from the gas phase is the dominant source of aqueous $^\bullet$OH.

To extrapolate ^{3}C* concentrations determined by SYR, we first fitted measured $P_{3C^*,SYR}$ versus DOC for each sample type to obtain the slope $\Delta P_{3C^*,SYR}/\Delta DOC$ (Fig. S29b), whose values are shown in Table S10. We then use these slopes to calculate $P_{3C^*,SYR}$ in ambient PM conditions with the estimated DOC concentration in ALW, which is calculated as the product of the average ratio of DOC to PM mass/water

mass ratio for each sample type (Table S10) and the particle mass concentration. We estimate the pseudo-first order rate constant for the organic sink of $^3C^*$ using the product of [DOC] and the second-order rate constant of DOC reacting with and quenching $^3C^*$ determined by SYR ($k_{rxn+Q,3C^*,SYR}$). For the bulk of our current samples, we use $k_{rxn+Q,3C^*,SYR}$ values from our previous work (Ma et al., 2023a): for the Win-Spr samples we use the Davis winter particle extracts (WIN), while for FBB and ABB samples, we use the rate constant from the summer wildfire sample (SUM). For the Sum-Fall samples, we use a rate constant obtained from fitting all of our current samples (Fig. S23b). The rate constants used are also shown in Table S10. $^3C^*$ concentrations are then calculated with:

$$[^3C^*] = \frac{P_{3C*}}{k'_{3C*}} = \frac{\Delta P_{3C*}/\Delta DOC \times [DOC]}{k_{3C*+O2}[O_2] + k_{rxn+Q,3C*}[DOC]} \tag{S5}$$

where k_{3C^*+O2} is the second-order rate constant of $^3C^*$ reacting with dissolved oxygen and [O_2] is the dissolved oxygen concentration. The DOC values in ambient PM condition are converted to particle mass/water mass ratios using the average ratio between DOC and PM mass to water mass ratio (DOC/(PM/H_2O)) for each sample type (Table S10). We predict [$^3C^*$]$_{PTA}$ in ALW using the same method but different values for the triplet production rate ($\Delta P_{3C^*,PTA}/\Delta DOC$) and triplet sink ($k_{rxn+Q,3C^*}$) (Table S10). Predictions for the SYR- and PTA-determined triplet concentrations as a function of PM mass/water mass ratio are in Figure S30.

The method we use to extrapolate $^1O_2^*$ to ALW conditions is similar to what we do for $^3C^*$. First, we fit P_{1O2*} against DOC for each sample type to obtain the slopes ($\Delta P_{1O2*}/\Delta DOC$) (Fig. S28a and Table S10). Next, we need to consider that since $^3C^*$ is the precursor of $^1O_2^*$, the triplet concentration will affect production of $^1O_2^*$. Therefore, in addition to acting as a source of singlet oxygen, DOC also affects $^1O_2^*$ in two other ways: (1) DOC is a direct sink for $^1O_2^*$ and (2) DOC suppresses $^1O_2^*$ production by quenching $^3C^*$. To quantify the first of these effects, we use an estimated average rate constant of DOC reacting with $^1O_2^*$ ($k_{1O2*+DOC}$) from previous work (Kaur et al., 2019; Ma et al., 2023a); the value of this second-order rate constant is 1.0×10^5 (L (mol C)$^{-1}$ s^{-1}), assuming independent of the sample type. We then take the product of this rate constant with the DOC concentration under ALW conditions to calculate the pseudo-first order rate constant $k'_{1O2*,DOC}$. For the second effect, we apply k_{3C^*+DOC} determined from $^1O_2^*$ data in our previous work. Note that k_{3C^*+DOC} values determined from $^1O_2^*$ are different from k_{3C^*+DOC} determined by SYR or PTA. The latter represents the impact of DOC on the oxidizing triplet pool, while the former represents the total triplet pool, i.e., triplets that can react with $^1O_2^*$. We then calculate [$^1O_2^*$] with (Ma et al., 2023a):

$$[^1O_2^*] = \frac{\frac{\Delta P_{1O2*}}{\Delta DOC} \times [DOC]}{1 + \frac{k_{3C*+DOC}[DOC]}{k_{3C*+O2}[O_2]}} / (k'_{H2O} + k_{1O2*+DOC}[DOC]) \qquad (S6)$$

where k'_{H2O} is the first-order rate constant for loss of $^1O_2^*$ in H_2O (2.2×10^5 s^{-1}; (Bilski et al., 1997)). The concentrations of singlet oxygen as a function of DOC are then transformed to a function of PM mass/water mass ratio using the relationships between these independent variables (Table S10). Predictions for the singlet oxygen concentration as a function of PM mass/water mass ratio are shown in Figure S29.

Figure S31 shows the predicted photooxidant concentrations for each sample type under aerosol liquid water conditions at 1 µg PM/µg H_2O. These concentrations are all normalized to the same photon flux condition (i.e. j_{2NB} = 0.07 s^{-1}). To consider the effect of actinic flux, we use the average estimated j_{2NB} values for each sample type (Table S9) to correct the photooxidant concentrations. These corrected values are shown in Figure 8.

Table S10. Parameters used to extrapolate photooxidant concentrations to ALW conditions

Parameters			Win-Spr	Sum-Fall	FBB	ABB
Average DOC/(PM/H$_2$O) (mol C L^{-1})/(µg PM/µg H$_2$O)			13.6	8.9	26.1	21.3
$^\bullet$OH	Gas-phase mass transport[a]	Gas-phase [OH] (molecular cm^{-3})	1×10^6			
		Mass accommodation coefficient α	1.0			
	$\Delta P_{OH}/\Delta DOC$ (M s^{-1}/(mol C L^{-1})[b]	WIN	1.5 × 10^{-6}			
		SUM	2.0 × 10^{-6} for DOC > 0.045 mol C L^{-1}			
			See SI in Ma et al. (2023a) for values at lower DOC			
	$k_{rxn+Q,OH}$ (L (mol C)$^{-1}$ s^{-1})		2.7 × 10$^{8\ c}$			
^{1}O$_2$*	$\Delta P_{1O2*}/\Delta DOC$ (M s^{-1}/(mol C L^{-1})		6.6 × 10^{-5}	3.2 × 10^{-5}	7.1 × 10^{-5}	4.0 × 10^{-5}
	$k_{rxn+Q,3C*}$ (L (mol C)$^{-1}$ s^{-1})		0.47 × 10^7 (WIN)[d]	1.2 × 10^7 (All)[e]	2.1 × 10^7 (SUM)[d]	
	$k_{DOC+1O2*}$ (L (mol C)$^{-1}$ s^{-1})		1.0 × 10$^{5\ f}$			
^{3}C*$_{SYR}$	$\Delta P_{3C*}/\Delta DOC$ (M s^{-1}/(mol C L^{-1})		8.4 × 10^{-5}	1.8 × 10^{-5}	7.5 × 10^{-5}	3.8 × 10^{-5}
	$k_{rxn+Q,3C*}$ (L (mol C)$^{-1}$ s^{-1})		7.6 × 10^7 (WIN)[d]	7.2 × 10^7 (All)[e]	12 × 10^7 (SUM)[d]	
^{3}C*$_{PTA}$	$\Delta P_{3C*}/\Delta DOC$ (M s^{-1}/(mol C L^{-1})		4.9 × 10^{-5}	0.61 × 10^{-5}	2.8 × 10^{-5}	1.4 × 10^{-5}
	$k_{rxn+Q,3C*}$ (L (mol C)$^{-1}$ s^{-1})		5.7 × 10^7 (WIN)[d]	7.4 × 10^7 (All)[e]	6.6 × 10^7 (SUM)[d]	

[a] To calculate the rate of gas-phase mass transport, we consider both gas-phase diffusion as well as interfacial transport. We assume the particle radius is 0.5 µm at 1 µg PM/µg H$_2$O and that the size quantitatively increases as the water content of the particles increases (Kaur et al., 2019).

[b] Values from our previous work (Ma et al., 2023a), using either the winter sample data (WIN) or the summer sample data (SUM). The final P_{OH} values used for extrapolation in this work is the average P_{OH} values of the WIN and SUM at a given PM mass/water mass ratio.

[c] Value is calculated as the average of slopes of k'_{DOC} with DOC in winter and summer samples from our previous work (Ma et al., 2023a).

[d] Values from our previous work (Ma et al., 2023a), using either the winter sample data (WIN) or the summer sample data (SUM).

[e] Values are calculated from the hyperbolic regressions shown in Figure S23, which use all samples from this work as well as the WIN and SUM samples from our previous work (Ma et al., 2023a).

[f] Second-order rate constant for loss of ^{1}O$_2$* by DOC. The value is estimated using the same approach from Kaur et al. (2019) but is lower than their value of 8.2 × 10^5 (L (mol C)$^{-1}$ s^{-1}.
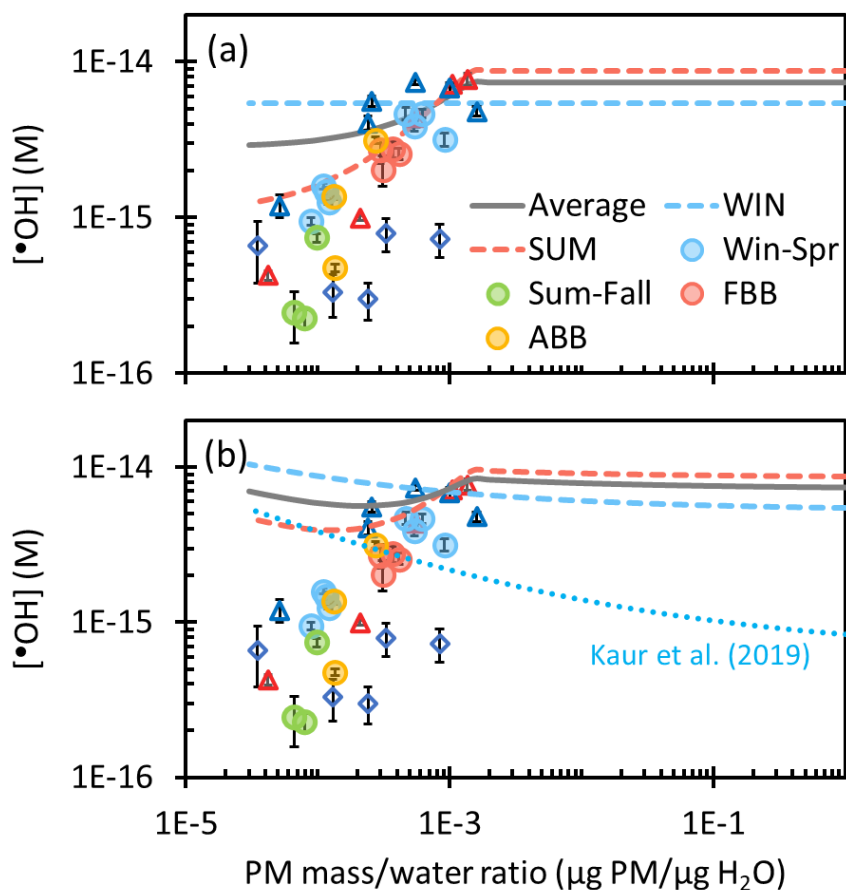
Figure S27. •OH concentration as a function of particle mass/water mass ratio calculated with (a) only aqueous •OH production and (b) •OH from both aqueous reactions and mass transport from the gas phase (Kaur et al., 2019) using a gas-phase •OH concentration of 1×10^6 mlc cm^{-3}. Circles are measured values. Previous measurements and extrapolations by Ma et al. (2023a) for Davis winter (WIN, blue) and summer wildfire (SUM, red) particle extracts are shown with triangles and dashed lines, while previous measurements and extrapolation by Kaur et al. (2019) for Davis winter particle extracts are shown with blue open diamonds and a dotted line. The grey line represents the average WIN and SUM •OH kinetics extrapolated to ALW conditions; this is our recommended prediction for all of the seasonality samples studied in the current work.
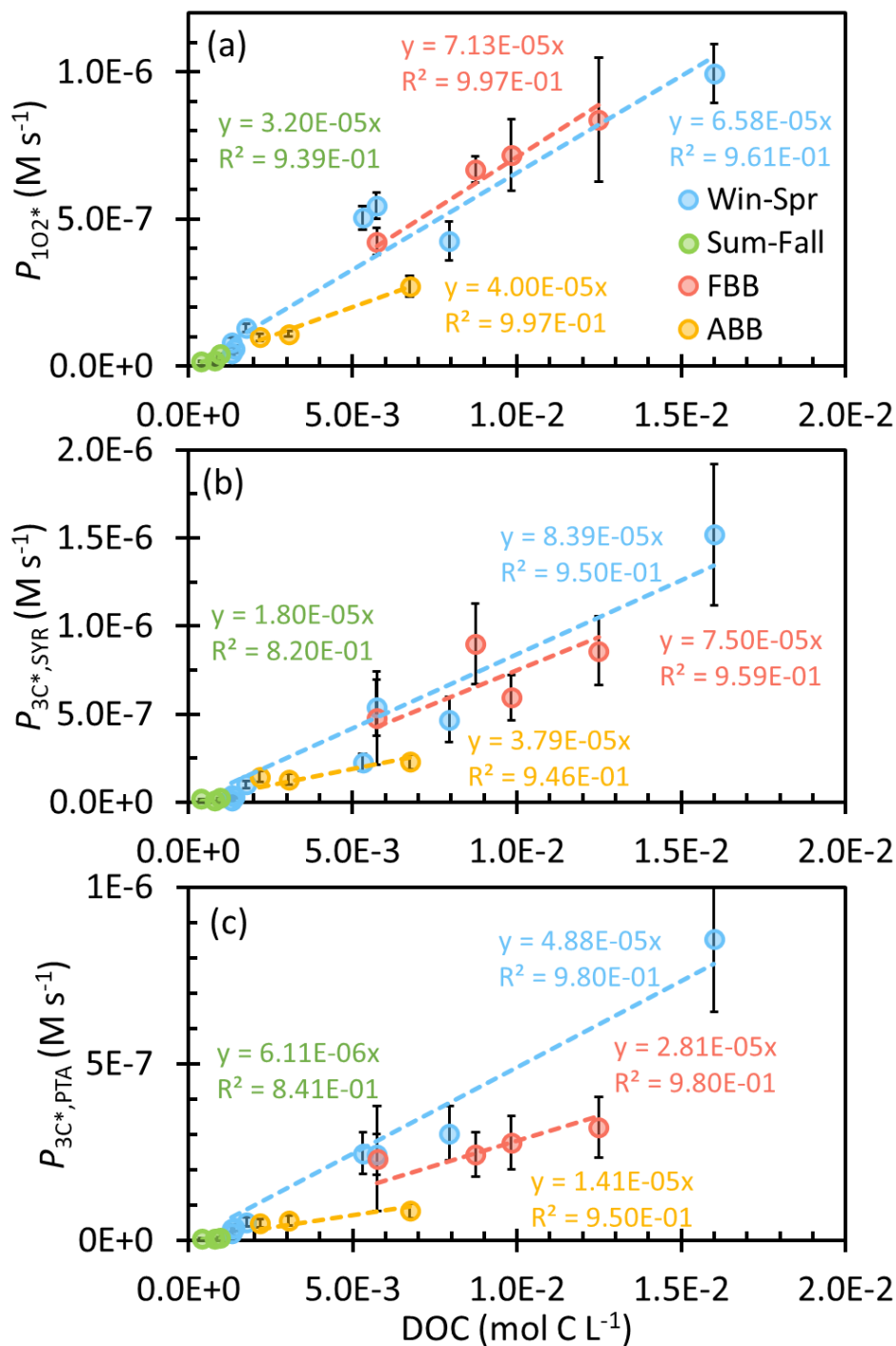
Figure S28. Production rates of (a) $^1O_2^*$ and $^3C^*$ determined by (b) SYR or by (c) PTA as a function of DOC. Dashed lines represent linear regressions (with *y*-intercepts fixed at zero) for each sample type.
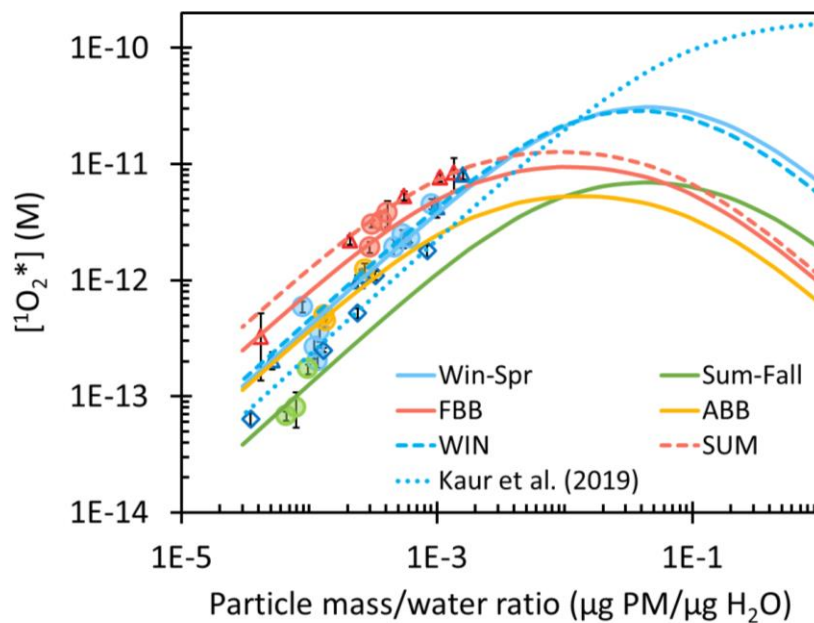
Figure S29. Dependence of $^1O_2^*$ concentrations for each sample type on particle mass/water mass ratio. Circles are measured values, while lines are extrapolations to ALW conditions. Previous measurements and extrapolations by Ma et al. (2023a) for Davis winter (WIN, blue) and summer wildfire (SUM, red) particle extracts are shown by triangles and dashed lines, while previous measurements and extrapolation by Kaur et al. (2019) for Davis winter particle extracts are shown with blue open diamonds and a dotted line.
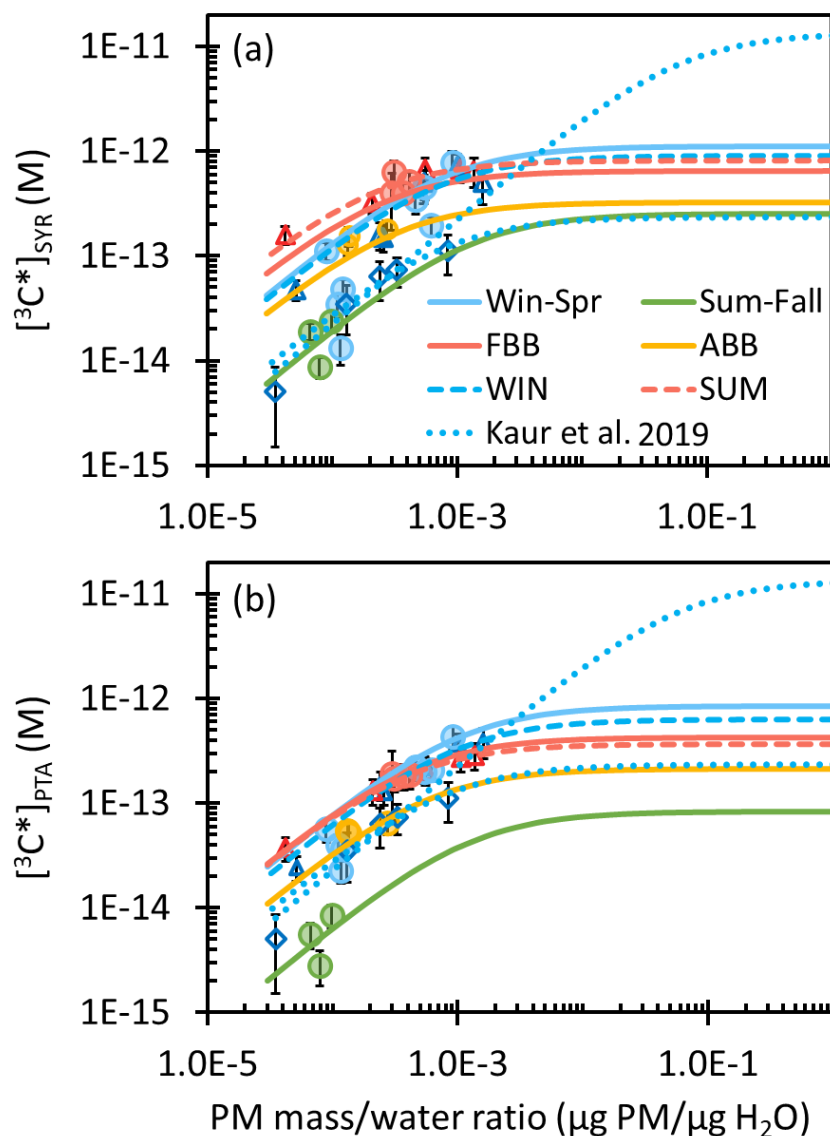
Figure S30. Dependence of ^{3}C* concentration for each sample type determined by (a) SYR and (b) PTA on particle mass/water mass ratio. Circles are measured values, while lines are extrapolations to ALW conditions based on equation S5. Previous measurements and extrapolations by Ma et al. (2023a) for Davis winter (WIN, blue) and summer wildfire (SUM, red) particle extracts are shown by triangles and dashed lines, while previous measurements and extrapolation by Kaur et al. (2019) for Davis winter particle extracts are shown with blue open diamonds and dotted lines.
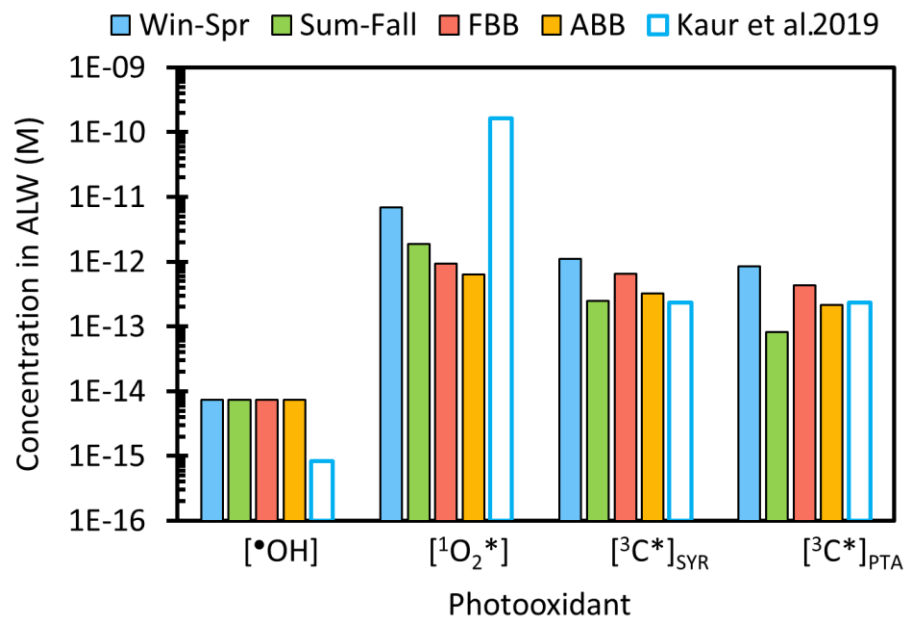
Figure S31. Predicted photooxidant concentrations for each sample type under aerosol liquid water conditions (1 µg PM/µg H_2O) normalized to the same actinic flux condition of midday on the winter solstice in Davis. Previous extrapolations made for Davis winter particle extracts are shown in open bars, where $^3C^*$ is the lower-bound estimate (Kaur et al., 2019).

References

Anastasio, C. and McGregor, K. G.: Chemistry of fog waters in California's Central Valley: 1. In situ photoformation of hydroxyl radical and singlet molecular oxygen, Atmos. Environ., 35(6), 1079–1089, doi:10.1016/S1352-2310(00)00281-8, 2001.

Bilski, P., Holt, R. N. and Chignell, C. F.: Properties of singlet molecular oxygen in binary solvent mixtures of different polarity and proticity, J. Photochem. Photobiol. A, 109(3), 243–249, doi:10.1016/S1010-6030(97)00147-0, 1997.

Canonica, S. and Laubscher, H.-U.: Inhibitory effect of dissolved organic matter on triplet-induced oxidation of aquatic contaminants, Photochem. Photobiol. Sci., 7(5), 547, doi:10.1039/b719982a, 2008.

Galbavy, E. S., Ram, K. and Anastasio, C.: 2-Nitrobenzaldehyde as a chemical actinometer for solution and ice photochemistry, J. Photochem. Photobiol. A, 209(2-3), 186–192, doi:10.1016/j.jphotochem.2009.11.013, 2010.

Kaur, R. and Anastasio, C.: First measurements of organic triplet excited states in atmospheric waters., Environ. Sci. Technol., 52(9), 5218–5226, doi:10.1021/acs.est.7b06699, 2018.

Kaur, R., Labins, J. R., Helbock, S. S., Jiang, W., Bein, K. J., Zhang, Q. and Anastasio, C.: Photooxidants from brown carbon and other chromophores in illuminated particle extracts, Atmos. Chem. Phys., 19(9), 6579–6594, doi:10.5194/acp-19-6579-2019, 2019.

Ma, L., Worland, R., Jiang, W., Niedek, C., Guzman, C., Bein, K. J., Zhang, Q. and Anastasio, C.: Predicting photooxidant concentrations in aerosol liquid water based on laboratory extracts of ambient particles, EGUsphere [preprint], doi:10.5194/egusphere-2023-566, 2023a.

Ma, L., Worland, R., Tran, T. and Anastasio, C.: An evaluation of probes to measure oxidizing triplet excited states in aerosol liquid water, Environ. Sci. Technol., 57(15), 6052–6062, doi:10.1021/acs.est.2c09672, 2023b.

McNeill, K. and Canonica, S.: Triplet state dissolved organic matter in aquatic photochemistry: reaction mechanisms, substrate scope, and photophysical properties., Environ. Sci. Process. Impacts, 18(11), 1381–1399, doi:10.1039/c6em00408c, 2016.

Rolph, G., Stein, A. and Stunder, B.: Real-time Environmental Applications and Display sYstem: READY, Environ. Model. Softw., 95, 210–228, doi:10.1016/j.envsoft.2017.06.025, 2017.

Ross, F. and Ross, A. B.: Selected specific rates of reactions of transients from water in aqueous solution. III. Hydroxyl radical and perhydroxyl radical and their radical ions, Historical Energy Database (United States)., 1977.

Smith, J. D., Kinney, H. and Anastasio, C.: Aqueous benzene-diols react with an organic triplet excited state and hydroxyl radical to form secondary organic aerosol., Phys. Chem. Chem. Phys., 17(15), 10227–10237, doi:10.1039/c4cp06095d, 2015.

Stein, A. F., Draxler, R. R., Rolph, G. D., Stunder, B. J. B., Cohen, M. D. and Ngan, F.: Noaa's HYSPLIT atmospheric transport and dispersion modeling system, Bull. Amer. Meteor. Soc., 96(12), 2059–2077, doi:10.1175/BAMS-D-14-00110.1, 2015.

Tratnyek, P. G. and Hoigne, J.: Oxidation of substituted phenols in the environment: a QSAR analysis of rate constants for reaction with singlet oxygen, Environ. Sci. Technol., 25(9), 1596–1604, 1991.

Wenk, J., von Gunten, U. and Canonica, S.: Effect of dissolved organic matter on the transformation of contaminants induced by excited triplet states and the hydroxyl radical., Environ. Sci. Technol., 45(4), 1334–1340, doi:10.1021/es102212t, 2011.